

# Signal Processing in Magnetoencephalography

Jiri Vrba and Stephen E. Robinson

*CTF Systems Inc., A subsidiary of VSM MedTech Ltd., 15-1750 McLean Avenue, British Columbia V3C 1M9, Port Coquitlam, Canada*

The subject of this article is detection of brain magnetic fields, or magnetoencephalography (MEG). The brain fields are many orders of magnitude smaller than the environmental magnetic noise and their measurement represent a significant metrological challenge. The only detectors capable of resolving such small fields and at the same time handling the large dynamic range of the environmental noise are superconducting quantum interference devices (or SQUIDs). The SQUIDs are coupled to the brain magnetic fields using combinations of superconducting coils called flux transformers (primary sensors). The environmental noise is attenuated by a combination of shielding, primary sensor geometry, and synthetic methods. One of the most successful synthetic methods for noise elimination is synthetic higher-order gradiometers. How the gradiometers can be synthesized is shown and examples of their noise cancellation effectiveness are given. The MEG signals measured on the scalp surface must be interpreted and converted into information about the distribution of currents within the brain. This task is complicated by the fact that such inversion is non-unique. Additional mathematical simplifications, constraints, or assumptions must be employed to obtain useful source images. Methods for the interpretation of the MEG signals include the popular point current dipole, minimum norm methods, spatial filtering, beamformers, MUSIC, and Bayesian techniques. The use of synthetic aperture magnetometry (a class of beamformers) is illustrated in examples of interictal epileptic spiking and voluntary hand-motor activity. © 2001 Elsevier Science

Magnetoencephalography (MEG) is a discipline concerned with detection and interpretation of magnetic fields produced by the human brain. It is a relatively new field, even though the detection of electromagnetic activity of the human brain has a long history. The electroencephalogram was first measured in 1929 (1) and its magnetic counterpart, the magnetoencephalogram, was first recorded 40 years later, in 1968 (2), using room temperature coils. Further progress in MEG required more sensitive detectors of magnetic fields,

which fortunately become available in 1964 (3, 4), shortly after the discovery of the Josephson effect in 1962 (5). These highly sensitive magnetic detectors are based on superconducting and quantum phenomena and are called SQUIDs (superconducting quantum interference device). SQUIDs were first used for MEG in 1972 (6). After this pioneering work, the field of MEG developed first by using single-channel devices, followed by somewhat larger systems with 5 to 7 channels in the mid- 1980s, then systems with 20 to 40 sensor arrays in the late 1980s and early 1990s, and finally the first helmet MEG systems were introduced in 1992. Present-day MEG systems have several hundreds channels in a helmet arrangement and operate in either sitting or supine position.

In addition to MEG, magnetic signals were also detected from other body organs (7), e.g., heart, eye, stomach, small intestine, skeletal muscles, peripheral nerves, fetal heart, fetal brain, lungs. However, so far the most important application of biomagnetism has been to the brain and the MEG started intense technological development in low-noise multichannel magnetic detection and led to the establishment of several commercial suppliers (8–10). It is interesting to note that during the 22-year period from 1970 to 1992 only about 1000 SQUID sensors were produced and used in all applications (7) (including nonbiomagnetic applications). However, since the introduction of the first helmet systems in 1992, nearly 10,000 SQUID sensors have been installed in approximately 60 MEG helmet systems now operating around the world.

MEG measurements span a frequency range from about 10 mHz to 1 kHz (or perhaps as low as 1 mHz for sleep studies) and field magnitudes from about 10 fT for spinal cord signals to about several picotesla for brain rhythms (11). To appreciate how small the MEG signals are, it should be recalled that the Earth's field

magnitude is about 0.5 mT and the urban magnetic noise about 1 nT to 1  $\mu$ T, or about a factor of 1 million to 1 billion larger than the MEG signals. Such large differences between signal and noise demand noise cancellation with extraordinary accuracy.

MEG signals are measured on the surface of the head and they reflect the current flow in the functioning brain. The cortex (Fig. 1a) contains well-aligned pyramidal cells, which consist of dendrites, cell body, and an axon and there are approximately  $10^5$  to  $10^6$  cells in an area of about 10 mm<sup>2</sup> of cortex (12). There are many connections between various parts of the brain mediated by nerve fibers which are connected to dendrites and cell bodies via synapses. In the whole brain there are approximately  $10^{10}$  cells and about  $10^{14}$  synaptic connections.

Because of ionic exchange between the cell and its surroundings, the equilibrium between diffusion processes and electrical forces establishes negative potentials of about -70 mV within the cell (13). Cell stimulation (chemical, electrical, or even mechanical) can cause alteration of the cell's transmembrane potential and can lead to cell depolarization (or hyperpolarization). Such changes can occur, e.g., at the synapse, when neurotransmitters are released. Because the cell is conductive, the depolarization (or hyperpolarization) causes current flow within the cell (called the impressed or intracellular current) and a return current outside the cell (called volume or extracellular current).

The dendritic current due to cell depolarization (or hyperpolarization) flows roughly perpendicular to the cortex. However, the cortex is convoluted with numerous sulci and gyri and, depending on where the cell stimulation occurred, the current flow can be either tangential or radial to the scalp surface (Fig. 1b). If the brain could be modeled as a uniform conducting sphere, then due to symmetry, only the tangential currents would produce fields outside the sphere (14) (Figs. 1c

and e) and the radial currents would produce no magnetic fields (Fig. 1d). If the magnetic detectors were radial to the head, then MEG would be mostly sensitive to the impressed intracellular currents, while EEG would detect the return volume currents.

Current flow within a single cell is too small and cannot produce observable magnetic fields outside the scalp. For fields to be detectable, it is necessary to have nearly simultaneous activation of a large number of cells, typically  $10^4$  to  $10^5$  (15). Generally, the MEG sources are distributed; however, activation of even large numbers of cells can often be assumed spatially small and can be modeled by a point equivalent current dipole (16). As an example, consider auditory evoked fields (AEFs) as in Fig. 19. Such fields typically yield equivalent current dipole magnitudes in the range 20 to 80 nA·m (18). It was shown that the current dipole density in the brain tissue is nearly constant and ranges from about 0.5 to 2 nA·m/mm<sup>2</sup> (17), which for our AEF dipole magnitude translates to the order of 1 cm<sup>2</sup> of activated cortical tissue. For such a relatively small activation area, approximation of the equivalent current dipole is satisfactory.

MEG measures the distribution of magnetic fields on the two-dimensional head surface. However, the required information is usually a three-dimensional distribution of currents within the brain. Unfortunately the field inversion problem is nonunique and MEG data must be supplemented by additional information, physiological constraints, or mathematical simplifications. One way to supply more information is to also use EEG (see Section 3). Both MEG and EEG measure the same sources of neuronal activity and their information is complementary (19). Additional information to assist field inversion can also be supplied by other imaging techniques. For structural information one can use magnetic resonance imaging (MRI) and computed axial tomography (CAT) and for functional information one

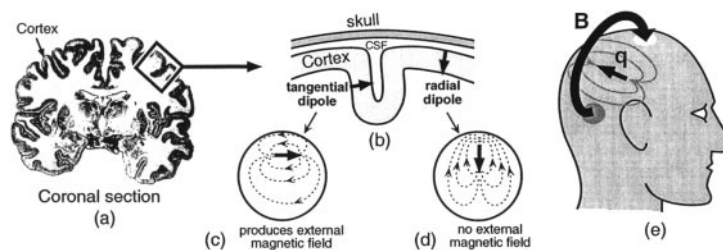


**FIG. 1.** Origin of the MEG signal. (a) Coronal section of the human brain. Cortex is indicated by dark color. The primary currents flow roughly perpendicular to the cortex. (b) The cortex has numerous sulci and gyri and its convoluted nature gives rise to the currents flowing either tangentially or radially relative to the head. The head can be approximated by a spherical conducting medium. (c) Tangential currents will produce magnetic fields that are observable outside the head. (d) Radial currents will not produce magnetic fields outside the head. (e) Magnetic fields due to cortical sources will exit and reenter the scalp.

can use positron emission tomography (PET), single-photon emission computed tomography (SPECT), and functional MRI (fMRI).

A typical MEG system is a complex installation and a schematic diagram is shown in Fig. 2. The SQUID detectors of magnetic field are housed in a cryogenic container called a dewar, which is usually mounted in a movable gantry for horizontal or seated positions. The subject or patient is positioned on an adjustable bed or chair. The SQUID system and patient may or may not be positioned in a shielded room. At present, the majority of installations use shielded rooms; however, progress is being made toward unshielded operations. The MEG measurement is usually supplemented by EEG and both MEG and EEG signals are transmitted from the shielded room to the SQUID and processing electronics and the computers for data analysis and archiving. The MEG system also contains stimulus delivery and its associated computer, which is synchronized with the data acquisition. The installation is completed with a video camera(s) and intercom for observation of and communication with the subject in the shielded room.

Even though the subject's head is inserted in the MEG helmet, there is still freedom to move it, and accurate measurement of the head position relative to the MEG sensors is necessary (the position information is used to register the MEG results relative to the brain anatomy, e.g., to MRI images). To accomplish accurate localization, various 3D digitizing methods may be used, e.g., (20), or the MEG system itself may be used for the head position determination. In that case three small coils are mounted on the subject's head at the nasion and preauricular points. The coils are energized from the computer; their magnetic signals are detected by the MEG system and used to determine the head position. The measuring procedure has submillimeter accuracy; however, the largest errors are caused by inaccurate coil placements or by head motion during the

measurement. It is estimated the overall head localization accuracy, considering all errors, is about 2 or 3 mm. Note that during the EEG measurement, the EEG electrodes are attached directly to the scalp surface in fixed positions relative to the head geometry and the question of head localization for the EEG purposes is not an issue (however, the electrode positions must be known accurately and should be digitized).

Photographs of a 151-channel MEG system (8) for horizontal and seated operation are shown in Fig. 3.

The MEG measurement process includes diverse technologies ranging from superconducting sensors, to analogue and digital SQUID electronics, to computer data acquisition. This procedure involves frequencies ranging from millihertz to more than a gigahertz, as shown in Fig. 4. Different frequency ranges are pointed out during the discussion of relevant MEG system components.

The article is organized as follows: Detection of the brain magnetic fields is discussed in Section 1. Section 1.1 outlines principles of SQUID sensors and Section 1.2 introduces flux transformers and compares their performance. Section 1.3 discusses how the processing electronics works, explains how SQUIDS are controlled by the electronics and what preprocessing and real-time processing tasks are performed by the electronics, and discusses data collection issues and examples. Section 1.4 describes the cryogenics required for the operation of SQUID sensors. Environmental noise cancellation is necessary for successful MEG operation. Noise cancellation methods and the system requirements for their successful performance are discussed in Section 2. Section 3 briefly outlines EEG and its integration with MEG. Section 4 discusses what is done with the measured MEG data and how the information about sources within the brain is extracted.

The material presented in this article has general validity; however, when discussing specific details of the instrumentation CTF's MEG system (8) is used as an example because the authors are most familiar with it.

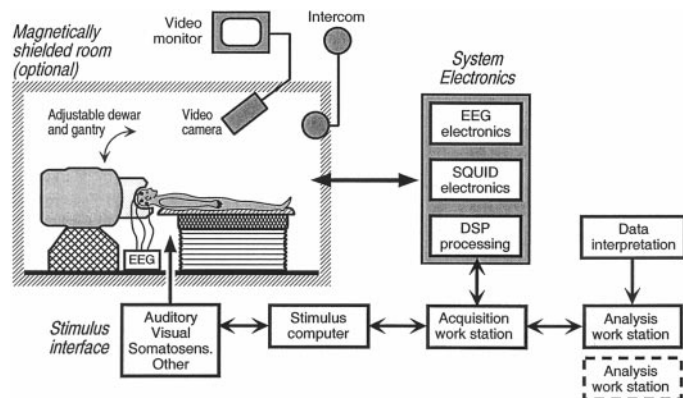


FIG. 2. Schematic diagram of an MEG installation (8).

## 1. SENSING OF MAGNETIC FIELDS

High-quality detection of brain magnetic fields is the first step in the MEG signal processing chain. The measured brain fields are small and the only detectors with adequate sensitivity are SQUID sensors. A schematic diagram of a typical SQUID magnetometer is shown in Fig. 5.

SQUID sensors exhibit high sensitivity to magnetic fields; however, their configuration is not best suited

for the direct detection of brain fields. SQUIDs are coupled to the brain fields by means of flux transformers. SQUIDs and their flux transformers are superconducting and must be operated at low temperatures, usually immersed in cryogen (either liquid He for low- $T_c$  SQUIDs or liquid N<sub>2</sub> for high- $T_c$  SQUIDs). The cryogen is contained in a thermally insulated container (dewar), which must be electromagnetically transparent so that the brain signals can reach the flux transformers and the SQUID detectors. SQUID signals are transmitted to room temperature and amplified, before being subjected to processing by the SQUID electronics. The signals from the SQUID electronics may be preprocessed in real time before they are acquired and manipulated by a computer. SQUID electronics and real-time processing electronics may be combined in one electronics system. Various elements of SQUID magnetometers are discussed in more detail in the following sections.

### 1.1. SQUID Sensors

The SQUID sensor is the heart of the MEG system and it provides high-sensitivity detection of small MEG signals. The most popular types of SQUIDs are dc and rf SQUIDs, deriving their names from the method of their biasing. The operation of SQUIDs is described briefly in this section; a more detailed description of their operation can be found in the literature [see, e.g., an excellent review (21)].

The modern commercial MEG instrumentation uses dc SQUIDs implemented in low-temperature superconducting materials (usually Nb). The dc SQUID can be

modeled as a superconducting ring interrupted by two resistively shunted Josephson junctions as in Fig. 6a (3). Josephson junctions are superconducting quantum mechanical devices that allow passage of currents with zero voltage, and when voltage is applied to them, they exhibit oscillations with frequency to voltage constant of about 484 MHz/ $\mu$ V. The resistive shunting causes the Josephson junctions to work in a nonhysteretic mode, which is necessary for low-noise operation (21). The SQUID sensors are usually made of thin films, even though in the past various 3D structures were used. An example of a thin-film dc SQUID, consisting of a square washer and Josephson junctions near the outside edge, is shown in Fig. 6b (22, 23).

The SQUID ring (or washer) must be coupled to the external world and to the electronics that operates it (see Fig. 7a). Because the SQUID impedance is low, it is usually matched to the room temperature preamplifier either by a cooled transformer (24) (shown in Fig. 6a), or a cooled resonant circuit (25). The impedance of the matching elements is designed to optimize the noise temperature of the preamplifier. When the dc SQUID is current biased, its  $I$ - $V$  characteristics is similar to that of a nonhysteretic Josephson junction and its critical current  $I_0$  is modulated by magnetic flux externally applied to the SQUID ring. The modulation amplitude is roughly equal to  $\Phi_0/L$  (21), where  $\Phi_0$  is the flux quantum with magnitude  $\approx 2.07 \times 10^{-15}$  Wb and  $L$  is inductance of the SQUID ring. The critical current is maximum for applied flux  $\Phi = n\Phi_0$  and minimum for  $\Phi = (n + 1/2)\Phi_0$ , and the dc SQUID  $I$ - $V$  characteristics are represented by heavy lines in Fig. 7b. When the SQUID

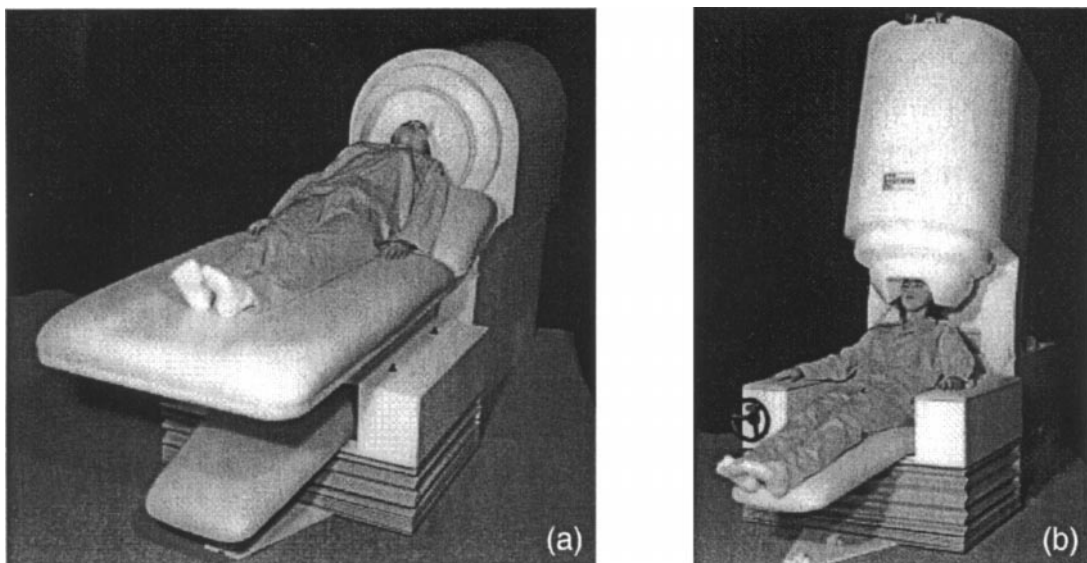
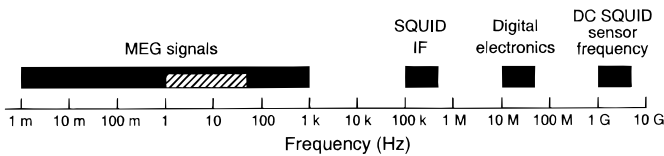


FIG. 3. Photograph of a 151-channel MEG system (8). (a) Horizontal operation. (b) Seated operation.

is biased by a dc current  $I_{DC} > I_0$ , the average value of the resulting voltage across the SQUID is modulated by externally applied flux between two extreme values  $V_1$  and  $V_2$  in Fig. 7b. For monotonically increasing flux the average SQUID voltage oscillates as in Fig. 7c with period equal to  $1 \Phi_0$ . The maximum magnitude of the voltage modulation is approximately  $\Delta V = \Phi_0 R / (2L)$ , where  $R/2$  is the parallel resistance of the two shunt resistors in Fig. 6a. Thus the SQUID flux-to-voltage transfer function is a multivalued periodic sinusoidal function and the SQUID is typically operated on its steep part where the magnitude of the transfer coefficient  $V_\Phi = \partial V / \partial \Phi$  is maximum.

Because the SQUID is biased above its critical current, there is a voltage applied to the Josephson junctions. The applied voltage causes the junctions to produce high-frequency oscillations at Josephson frequency (5), which for typical dc SQUIDs is of the order



**FIG. 4.** Frequencies needed for MEG signal processing. The brain signals range from millihertz to kilohertz, the magnetic SQUID detectors contain frequencies in the gigahertz range, and the SQUID electronics operates with frequencies in the hundreds of kilohertz and tens of megahertz. The shaded bar in the “MEG signals” indicates the range where the spontaneous MEG can be seen above the sensor noise without any processing or averaging.

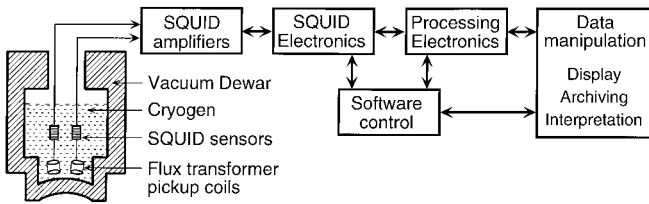


**FIG. 5.** Schematic diagram of a typical SQUID magnetometer.

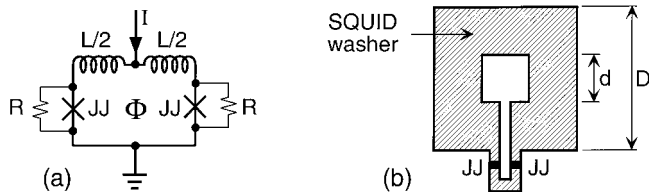


**FIG. 6.** Diagram of a typical thin-film dc SQUID. (a) Schematic diagram indicating inductance of the SQUID ring and shunting resistors to produce nonhysteretic Josephson junctions (the Josephson junctions are indicated by  $\times$ 's). (b) Diagram of a simple SQUID washer with Josephson junctions, JJ, near the outer edge.

of gigahertz. The oscillations are highly asymmetric and their average voltage is not zero. All voltages discussed in connection with Fig. 7 correspond to these average voltages.

The rf SQUIDs were popular in the early days of superconducting magnetometry because they required only one Josephson junction; however, in the majority of low- $T_c$  commercial applications, rf SQUIDs have been displaced by dc SQUIDs. In recent years, interest in rf SQUIDs has been renewed in connection with high- $T_c$  superconductivity. The rf SQUID consists of a superconducting inductor interrupted by one nonhysteretic Josephson junction, as in Fig. 7d. The SQUID is coupled to a tank circuit and the average voltage on the tank circuit is a measure of the flux applied to the SQUID (26, 27).

The behavior of rf SQUID current and flux is especially simple for  $LI_0 \gg \Phi_0$ . Assume that the SQUID has been cooled to the superconducting state in zero external field and the current and flux in the SQUID inductor are zero (zero flux state,  $n = 0$ ). Application of a small flux to the SQUID will give rise to a screening current in the SQUID inductor, but the flux inside the SQUID ring will remain essentially zero. As the applied flux slowly increases, the magnitude of the screening current also increases, while the flux remains close to zero. When the screening current reaches the critical value  $I_0$  of the Josephson junction, the junction momentarily switches into a resistive state and the SQUID jumps from the state  $n = 0$  to  $n = 1$ . For a monotonic flux increase this process repeats itself and results in periodic insertion of more flux quanta into the SQUID inductor.

Consider a SQUID ring threaded by flux  $\Phi_S$  and inductively coupled to a tank circuit. The tank circuit is excited at its resonant frequency by current  $I_{rf}$  and the current through the tank circuit inductor,  $L_T$ , is proportional to  $Q I_{rf}$ , where  $Q$  is the tank circuit quality factor. For small  $I_{rf}$  the rf flux coupled to the SQUID is small and the SQUID screening current oscillates around zero and the flux through the SQUID inductor remains roughly constant. In this regime the voltage  $V_{rf}$  on the tank circuit increases proportionally to  $I_{rf}$ , as in Fig. 7e for small  $I_{rf}$ . As the bias  $I_{rf}$  increases, it reaches a level at which the induced SQUID screening current magnitude at the rf peak reaches the critical current  $I_0$ , the flux transition occurs, and  $1 \Phi_0$  is either added or subtracted from  $\Phi_S$ . The flux transition will dissipate energy from the tank circuit and will reduce the tank circuit voltage magnitude and therefore the induced screening current in the SQUID ring.

It takes many rf cycles to replenish the dissipated energy and to restore the rf current through  $L_T$  to its original value, before the next quantum transition in

the SQUID ring is triggered. For larger  $I_{rf}$  biases, the current in the  $L_T$  recovers in fewer rf cycles; however, the average tank circuit voltage will remain constant (horizontal part of the  $V_{rf}$  vs  $I_{rf}$  characteristics in Fig. 7e). More detailed analysis reveals that as a function of the tank circuit bias  $I_{rf}$ , the  $V_{rf}$ -versus- $I_{rf}$  characteristics exhibit a series of plateaus and risers (21). Similar to the dc SQUIDs, the level at which the tank circuit is stabilized also depends on the dc flux threading the SQUID ring, being maximum for applied flux  $\Phi = n\Phi_0$  and minimum for  $\Phi = (n + 1/2)\Phi_0$ . In between the two extreme flux levels the tank circuit voltage changes linearly with the flux. For monotonically increasing applied flux, the tank circuit oscillates between its two extreme levels and the rf SQUID transfer function is a triangular periodic function of applied flux with periodicity of  $1 \Phi_0$ , as shown in Fig. 7f. The magnitude of the voltage triangles in Fig. 7f is (21)  $\Delta V = \omega_{rf} L_T \Phi_0 / (2M)$ , where  $\omega_{rf}$  is the rf frequency and  $M$  is mutual inductance between the tank circuit coil  $L_T$  and the SQUID ring. If  $LL_0 \approx \Phi_0$ , the voltage triangle height is optimized for  $k^2 Q \geq \pi/4$ , where  $k$  is the coupling constant between the SQUID inductor  $L$  and the tank inductor  $L_T$ ,  $k = M/\sqrt{LL_T}$ .

The magnetic field resolution of SQUID sensors is given by their noise performance which can be conveniently characterized in terms of the noise energy per unit bandwidth (21) (or energy sensitivity)

$$\varepsilon(f) = \frac{S_\Phi(f)}{2L}, \quad [1]$$

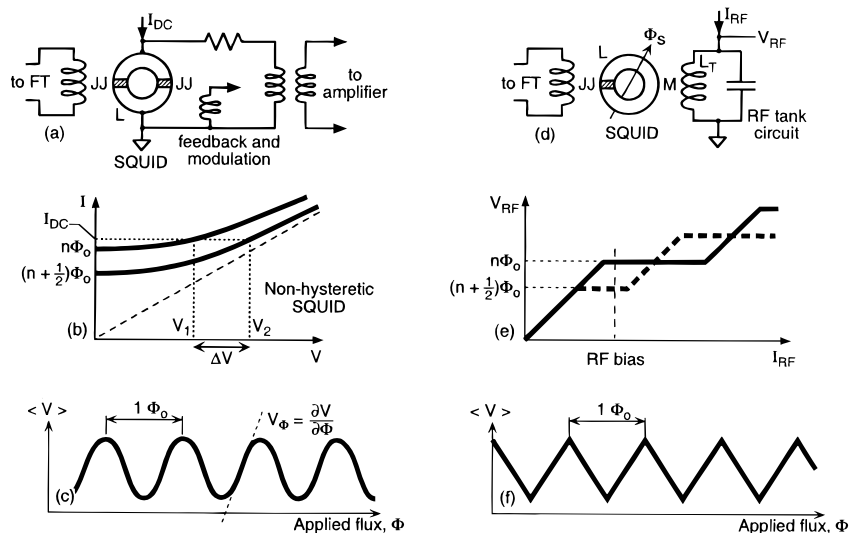


**FIG. 7.** SQUID sensors and their operating characteristics. (a) dc SQUID and its coupling circuitry; the Josephson junctions in the SQUID are assumed to be resistively shunted. (b) Current-voltage characteristics of a dc SQUID. (c) Flux (or field)-to-voltage transfer function of a dc SQUID. (d) rf SQUID and its coupling circuitry; (e) Mean tank voltage versus rf bias characteristics of a rf SQUID. (f) Flux-to-voltage transfer function of a rf SQUID.

where  $S_\Phi(f)$  is the spectral density of the flux noise. For dc SQUIDs the energy sensitivity was shown by simulations to be  $\varepsilon = 9k_B TL/R$  (31). For typical dc SQUIDs [e.g., in commercial biomagnetometers (29)] the energy sensitivity may be  $\varepsilon \approx 10^{-31} - 10^{-32}$  J/Hz and for typical rf SQUIDs operated in 30- to 50-MHz range  $\varepsilon \approx 5 \times 10^{-29}$  J/Hz (28, 31). Thus, for typical applications, the field sensitivity of dc SQUIDs is more than 10 times better than that of rf SQUIDs. Energy sensitivity achieved for experimental dc SQUIDs cooled to 0.3 K was  $\varepsilon \approx 3 \times 10^{-34}$  J/Hz  $\approx 3 \hbar$  (30), and for rf SQUIDs using cooled high-electron-mobility transistors as a pre-amplifier,  $\varepsilon \approx 3 \times 10^{-32}$  J/Hz (32).

In recent years, there has been significant progress in the development of high- $T_c$  SQUIDs, both dc and rf. These devices are usually constructed from  $YBa_2Cu_3O_{7-x}$  ceramics. High- $T_c$  SQUID magnetometers were shown to achieve noise levels below  $10$  fT/ $\sqrt{\text{Hz}}$  (33); however, their poorer low-frequency performance and difficulties with reproducible large-volume manufacturing do not yet make them suitable for large-scale MEG applications.

## 1.2. Flux Transformers

The purpose of flux transformers is to couple the SQUID sensors to the measured signals and to increase overall magnetic field sensitivity. Flux transformers are superconducting and consist of a pickup coil(s) which is exposed to the measured fields, leads, and a coupling

coil which inductively couples the flux transformer to the SQUID ring (see the left-hand inductors in Figs. 7a and 7d). Because the flux transformers are superconducting, they do not generate noise and their gain is noiseless.

The flux transformer pickup coils can have diverse configurations (Fig. 8). A single loop of wire acts as a magnetometer and is sensitive to the magnetic field component perpendicular to its area (Figs. 8a and 8b). Two magnetometer loops can be combined with opposite orientation and connected by the same wire to the SQUID sensor. Such configuration is sensitive only to the magnetic field changes across the device dimension and the pickup coils are called first-order gradiometers, (Figs. 8c–8e). Similarly, first-order gradiometers can be combined with opposing polarity to form second-order gradiometers (Figs. 8f and 8g) and second-order gradiometers can be combined to form third-order gradiometers (Fig. 8h). Other configurations are possible but not widely used in MEG practice (tangential gradient of tangential field, e.g., (c) or (d) tipped to its side, parallel planar gradiometers). The planar structures in Figs. 8a, 8b, 8d, and 8e permit thin-film construction and integration with the SQUID sensor on the same chip. The flux transformers in Fig. 8 are called hardware flux transformers, because they are directly constructed in hardware by interconnecting various coils. In Section 2 synthetic gradiometers are discussed.

An important function of flux transformers in MEG applications is to help reduce environmental noise. In an ideal noiseless situation, it would be sufficient to use magnetometers as in Figs. 8a and 8b. However, the magnetometers are sensitive not only to the near-field MEG signals but also to the fields generated by distant noise sources. For these reasons, the MEG systems usually employ some kind of gradiometer as a primary sensor. The gradiometers attenuate signals from distant sources and in effect behave as spatial high-pass filters (34). This can be understood by considering a

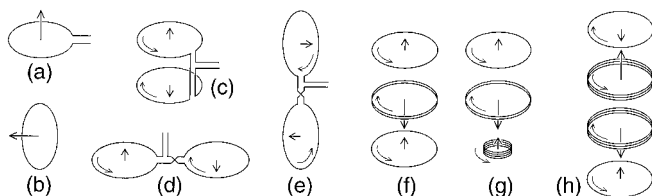


**FIG. 8.** Examples of hardware flux transformers for biomagnetic applications. The flux transformer orientation assumes that the scalp surface is at the bottom of the figure. (a) Radial magnetometer. (b) Tangential magnetometer. (c) Radial first-order gradiometer. (d) Planar first-order gradiometer. (e) Radial gradiometer for tangential fields. (f) Second-order symmetric gradiometer. (g) Second-order asymmetric gradiometer. (h) Third-order symmetric gradiometer.

dipolar magnetic source. The field of a dipole decays with distance,  $R$ , as  $1/R^3$ . The first gradient decays as  $1/R^4$ , and for each increase of the gradient order by 1 the decay exponent also increases by 1. Thus the gradients due to distant sources are reduced far more than the fields, while for the near (brain) sources the gradiometers and magnetometers have comparable sensitivities. Also, the attenuation of distant sources is better when the gradient order is high.

For these purposes the early single channel MEG detectors used second- or third-order hardware gradiometers, Figs 8f–8h. However, the hardware gradiometers are bulky, difficult to manufacture accurately, and also partially reduce the MEG signals. For these reasons, large-scale MEG instruments use only magnetometers or first-order gradiometers as primary sensors, and for effective noise cancellation, the higher-order gradiometers are synthesized in software or firmware (35).

Main types of hardware flux transformers used in commercial practice as primary sensors are magnetometers (Fig. 8a), radial gradiometers (Fig. 8c), and planar gradiometers (Fig. 8d). Their responses to an equivalent current dipole, (Fig. 9) were computed assuming that the current dipole is located below the points indicated by black arrows and the respective devices are scanned in a plane above the dipole.

The radial magnetometer produces a field map with one maximum and one minimum, symmetrically located on the dipole sides (Fig. 9a). The separation of the extrema,  $d$ , can be used to determine the dipole depth as  $d/\sqrt{2}$  (36). Directly above the dipole the radial field is zero. The radial gradiometer in Fig. 9b produces similar field pattern as the magnetometer, except that

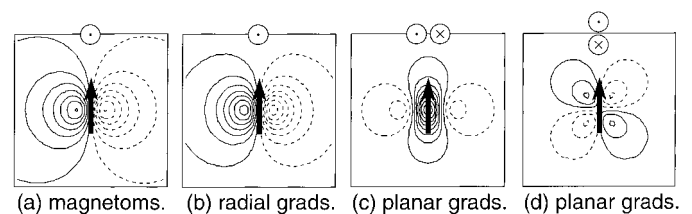


**FIG. 9.** Response to a point current dipole of the most frequently used hardware flux transformers. A tangential dipole is positioned 2 cm deep in a semi-infinite conducting space bounded by  $x_3 = 0$  plane and its field is scanned by the flux transformers positioned in  $x_3 = 0$  plane. Dimensions of each map are  $14 \times 14$  cm. Schematic top view of the flux transformers is shown in the upper part of each figure. Solid and dashed lines indicate different field polarities. (a) Radial magnetometers, Fig. 8a. (b) Radial gradiometers with 4-cm baseline, Fig. 8c. (c) Planar gradiometers with 1.5-cm baseline, Fig. 8d, aligned for maximum response. (d) Planar gradiometers with 1.5-cm baseline, Fig. 8d, aligned for minimum response.

the pattern is spatially tighter. This is because the gradiometer subtracts two field patterns measured at different distances from the surface of the scalp. The planar gradiometer field patterns in Figs. 9c and 9d are quite different from those of radial devices. If the two coils of the planar gradiometer were aligned perpendicular to the dipole, as in Fig. 9c, the planar gradiometer would exhibit a peak directly above the dipole; if the two coils were aligned parallel to the dipole, the planar gradiometer would read zero directly above the dipole and the map of its response would exhibit a weak, cloverleaf pattern. If two orthogonal planar gradiometers were positioned at the same location, their two independent components would determine orientation of the current dipole located directly under the gradiometers (37).

In the absence of noise, the detected field patterns in Fig. 9 could be transformed from one to another and there would be no practical difference between the devices. However in the presence of noise (Section 2) the situation is more complicated and the signal-to-noise ratios of different devices can differ significantly, resulting in significant performance differences. The ideas behind comparing different devices on the basis of their  $S/N$  ratios are illustrated in Fig. 10.

First, consider radial devices and ask whether we want gradiometers or magnetometers (the magnetometers can be thought of as gradiometers with infinitely long baseline) and what should the optimum gradiometer baseline (separation between the coils) be. It can be shown that the magnitude of the detected brain signal increases with gradiometer baseline (Fig. 10a) and the magnitude of the detected environmental noise also increases with increasing baseline (Fig. 10b) (38). Both the detected brain signal and detected environmental noise increase with increasing baseline, but since their functional dependencies are different, the  $S/N$  ratio peaks at a certain optimum baseline, (Fig. 10c). Since the  $S/N$  ratio is the most important operating parameter of MEG sensors, we should choose baselines corresponding to this optimum baseline, which is in the range of about 3 to 8 cm. Thus magnetometers are not optimal because their “baseline” is too long and as a result their  $S/N$  performance is inferior to that of radial gradiometers with optimum baseline.

To decide between radial and planar gradiometers, the noise has to be again considered. There are three major types of noise acting on the detector: white noise of the sensors, environmental noise, and brain noise. The brain noise is the brain signal due to the extended background brain activity. This background signal can be considered a noise when a specific location in the brain is investigated and signals from other brain regions are of no interest (e.g., during studies of evoked responses) (37). The brain noise is spatially correlated,

because different sensors measure contributions from the same regions of the brain. In many situations, however, the background brain activity is considered the signal and the argumentation based on the brain noise is irrelevant. If the environmental noise were the only noise acting on the detector, the planar gradiometers would clearly be suboptimal because their baselines are too short (about 1.4–1.6 cm) (see Fig. 10c).

To compare the performance of radial and planar gradiometers for white sensor noise and brain noise, it is assumed that the gradiometer arrays are used to localize one equivalent current dipole source (14) and the standard deviation of the source position,  $\sigma$ , is used as a measure of the device performance.  $\sigma$  is directly connected to confidence intervals and it is also related to the  $S/N$  ratio (inversely proportional to it). When only the random sensor noise acts on the gradiometers,  $\sigma$  values are shown in Fig. 10d as a function of the

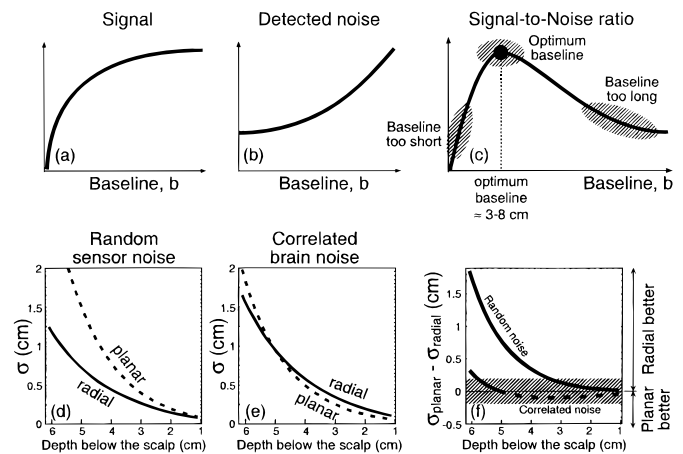


**FIG. 10.** Optimization of flux transformer noise performance and comparison of different flux transformer types: 150 channels, sensor shell radius  $r = 11$  cm, head radius  $r_{\text{head}} = 9.1$  cm. (a–c) Optimization of the radial gradiometer baseline: (a) radial gradiometer brain signal as a function of baseline length; (b) environmental noise detected by the radial gradiometer as a function of the baseline length; (c) signal-to-noise ratio as a function of the baseline. An optimum operating point exists at relatively short baselines. (d–f) Comparison of the standard deviation of the dipole localization error,  $\sigma$ , for planar and radial gradiometers in the presence of random or correlated brain noise; (d) planar and radial gradiometers, random noise,  $n_w = 5$  fT rms/ $\sqrt{\text{Hz}}$ , bandwidth = 100 Hz; (e) planar and radial gradiometers, correlated brain noise, bandwidth = 100 Hz, number of averages = 100, brain noise density detected by radial gradiometers,  $n_b = 30$  fT rms/ $\sqrt{\text{Hz}}$ , and planar gradiometers,  $n_p = 15$  fT rms/ $\sqrt{\text{Hz}}$ ; (f) difference between planar and radial standard deviations of the localization accuracy. The upper curve corresponds to the random sensor noise, the lower curve to the correlated brain noise. When the difference is positive, the radial gradiometers give smaller localization errors, and when the difference is negative, the planar gradiometers give smaller localization errors. The shaded band indicates the mechanical uncertainty of the localization and registration.

dipole depth below the scalp surface. For all investigated depths the standard deviation  $\sigma$  is larger for planar gradiometers than for radial gradiometers. The performance of planar gradiometers in this regime is worse than that of radial gradiometers because planar gradiometer signal strength decays faster with depth than radial gradiometers signal strength.

The magnitude of brain noise detected by different sensor types scales with the sensor ability to see more distant sources. Thus planar gradiometers with about 1.5-cm baseline will see about 50% of the brain noise that radial gradiometers with about 5-cm baseline see (37). If brain noise was used for calculation of  $\sigma$ , then the result would be as in Fig. 10e. In this case, because of the lower brain noise, the planar gradiometer  $\sigma$  is smaller than the radial gradiometer  $\sigma$  for source depths smaller than  $\approx 5$  cm. For deeper sources planar gradiometer  $\sigma$  becomes larger than radial gradiometer  $\sigma$ , again because planar gradiometers lose signal strength faster than radial gradiometers. Even though planar gradiometers produce smaller positioning errors than radial gradiometers for sources less than 5 cm deep, the differences between the two devices are small. This is emphasized in Fig. 10f, where the difference  $\sigma_{\text{planar}} - \sigma_{\text{radial}}$  is plotted as a function of depth for both the random sensor and correlated brain noise. When the difference is negative, planar gradiometers produce the better result (dashed line); when the difference is positive, radial gradiometers produce the better result (solid line). Also shown by the shaded band is the range of head positioning and MRI registration inaccuracies ( $\pm 0.2$  cm). The planar gradiometer advantage is overshadowed in this region of positioning inaccuracy and is not really important.

Based on environmental noise, it was shown that magnetometers have poorer  $S/N$  performance than radial gradiometers. The consideration of brain noise, when applicable, makes the magnetometer even more disadvantaged because they see about 30% more brain noise than radial gradiometers with about 5 cm baseline.

To conclude this section, the design of hardware gradiometers for optimum coupling to SQUID sensors is briefly outlined. To optimize a flux transformer, it is required that flux transferred to the SQUID loop (e.g., Fig. 7a) be maximized. To illustrate the optimization, consider a simple magnetometer flux transformer. The optimum field resolution is given by (31)

$$\delta B_{\text{mag}} = \frac{2\sqrt{2\varepsilon L_P}}{kA} \approx \frac{2(\mu_0\varepsilon)^{1/2}}{kr^{3/2}}, \quad [2]$$

where  $A$  is the pickup loop area,  $r$  is the radius of the

pickup loop,  $L_P$  is the pickup loop inductance,  $k$  is coupling constant between the SQUID and the flux transformer coupling coil,  $\mu_0$  is permeability of vacuum, and  $\varepsilon$  is the SQUID energy sensitivity (Eq. [2]). It was assumed during derivation of the right-hand side of Eq. [2] that the inductance of the pickup loop can be approximated by  $L_P \approx 5\mu_0 r$  (31). Eq. [2] indicates that the magnetometer resolution can be made arbitrarily small by increasing the radius  $r$  of the pickup coil. For a typical DC SQUIDS (e.g., in commercial MEG systems) the energy sensitivity may be  $\varepsilon \approx 10^{-31}$  to  $10^{-32}$  J/Hz,  $k \approx 0.7$  and the magnetometer with 1-cm diameter loop would exhibit sensitivity of  $\delta B_{\text{mag}} \approx 1$  to  $3 \text{ fT}/\sqrt{\text{Hz}}$ . The method of gradiometer sensitivity optimization is similar and terms describing inductive effects of various coils in the gradiometer flux transformer must be included in Eq. [2] (42). To enhance the flux transformer–SQUID resolutions, asymmetrical flux transformers as in Fig. 8g can be constructed, and if multiturn coils are used, the turns can be spaced to reduce the inductive loading.

Primary hardware gradiometers were discussed assuming that they are manufactured perfectly. Real gradiometers, however, are subject to different manufacturing errors: their coils may not have equal areas, coils could be tilted, there are parasitic loops in the gradiometer leads, or there could be pieces of bulk superconductor or normal metal in their vicinity. All these factors conspire to make the gradiometers sensitive not only to the designed gradients, but also to magnetic fields and/or their derivatives. These errors are called common mode and eddy current errors and they must be eliminated either by hardware or software balancing (42). Discussion of these problems and of corrective actions is outside the scope of this article.

### 1.3. SQUID Electronics

The SQUID transfer function is periodic (Fig. 7c) and to linearize it, the SQUID is operated in a feedback loop as a null detector of magnetic flux (25). Most SQUID applications use an analog feedback loop, as shown in Figs. 11a and 11b. A modulating flux with  $\pm 1/4 \Phi_0$  amplitude is applied to the SQUID sensor through the feedback circuitry. The modulation, feedback signal, and flux transformer output are superposed in the SQUID, amplified, and demodulated in a lock-in detector fashion. The demodulated output is integrated, amplified, and fed back as a flux to the SQUID sensor to maintain its total input close to zero. The modulation flux superposed on the dc SQUID transfer function is shown in Fig. 11d. and the modulation frequencies are typically several hundreds of kilohertz.

The analog feedback loop is not always adequate for

MEG operation. Even though MEG signals are relatively small and well behaved, the MEG system is also exposed to environmental noise, which increases demand on the MEG electronics system performance. Examination of the range of environmental signals observed during either shielded or unshielded operations indicates that for satisfactory MEG operation the SQUID system must exhibit large dynamic ranges, excellent interchannel matching, good linearity, and satisfactory slew rates. The exact parameters depend on whether the primary sensors are magnetometers or gradiometers and whether the system is operated unshielded or shielded (39). Typically, the dynamic ranges required for gradiometer primary sensors are about 22 and 27 bits for shielded and unshielded operation, respectively. Similar numbers for magnetometer primary sensors are 27 and 31 bits. The interchannel matching is especially important when the primary sensors are magnetometers, where for the shielded operation tens of microseconds, and for unshielded several 100-nanoseconds, synchronicity is required.

To accommodate the above requirements, the dynamic range of the SQUID feedback loop was extended by using the flux periodicity of the SQUID transfer function (40) and the loop was completed with a digital

integrator to ensure optimum interchannel matching (41) (see Fig. 11c). The extension of the dynamic range by using the flux periodicity of the SQUID transfer function works in the following manner: The loop is locked at a certain point on the SQUID transfer function and remains locked for the applied flux in the range of  $\pm 1 \Phi_0$ , (Fig. 11d). When this range is exceeded, the loop lock is released and the locking point is shifted by  $1 \Phi_0$  along the transfer function. The flux transitions along the transfer function are counted and are merged with the signal from the digital integrator to yield a 32-bit dynamic range. The linearity of the system was measured to be better than  $10^{-6}$  at a signal amplitude of  $1000\Phi_0$  (it is not known whether the linearity limit is due to the SQUIDS, electronics system, or measuring apparatus). The flux slipping concept can also be implemented using four-phase modulation (47), where the feedback loop jumps by  $\Phi_0/2$  and can also provide compensation for the variation of SQUID inductance with flux changes (which might be important for high- $T_c$  SQUID sensors).

MEG systems contain large numbers of MEG, EEG, and auxiliary channels and the architecture of the digital electronics must be designed to accommodate them.

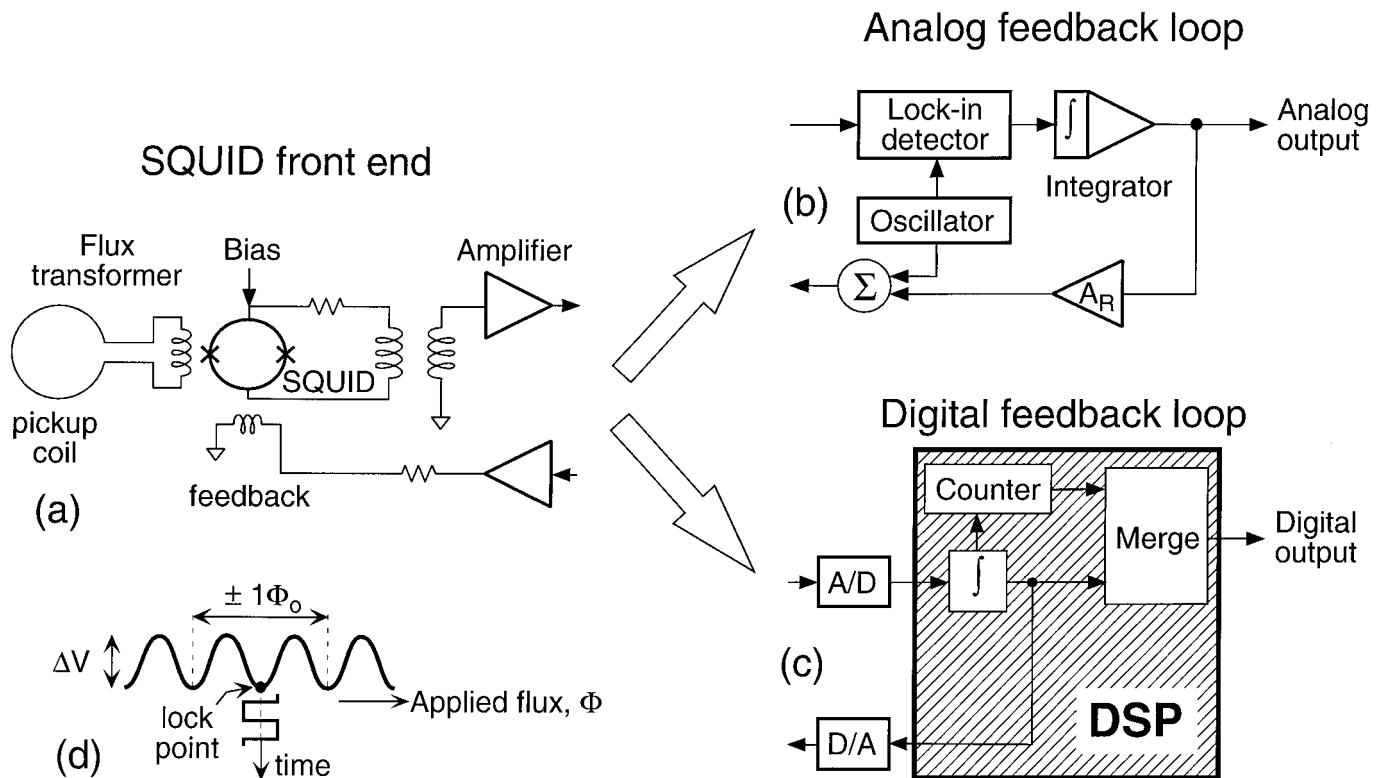


**FIG. 11.** SQUID within a feedback loop. (a) Coupling of SQUID sensor to the amplifier. (b) Analog feedback loop. (c) Digital feedback loop using digital signal processor (DSP). (d) Feedback loop modulation.

A block diagram of such a system is shown in Fig. 12 (43). The electronics consists of four major parts: MEG, EEG, peripheral interface unit (PIU), and DSP processor unit. The MEG unit is organized in banks; each bank can have up to 192 MEG channels (Fig 12 shows two banks with 384 MEG channels). The banks contain SQUID electronics as discussed above, control for SQUIDS, automated tuning and diagnostics, heaters, data communication interface, and digital processors for real-time computation tasks. MEG electronics and SQUIDS were designed for robust operation, exhibiting high immunity to rf interference, immunity to fluxing, and "set and forget" tuning.

The EEG subsystem has a similar modular design and can contain multiple channel units, each accommodating up to 32 EEG channels (composed of 24 unipolar channels and 8 either bipolar or unipolar channels). The EEG is digitized to 21 bits (using oversampling) and for convenience, similar to MEG, the EEG data word is also 4 bytes. The PIU is designed to accept or transmit signals to the peripheral equipment, stimulation equipment, head positioning, head shape digitization, and EEG electrode position measurement. The DAC units also double as function generators for a range of waveforms. Signals from the MEG, EEG, and PIU are transmitted by fiberoptic links to the DSP unit for preprocessing before the data are acquired by a host computer. The system allows for sample rates of up to 4 kHz with a total of 450 channels (higher sample rates up to 12 kHz are possible for smaller subsets of channels).

A more generalized block diagram of the MEG electronics, emphasizing its real-time and off-line processing capabilities, is shown in Fig. 13 (8). The Programmable Gate Array/Digital Signal Processor MEG

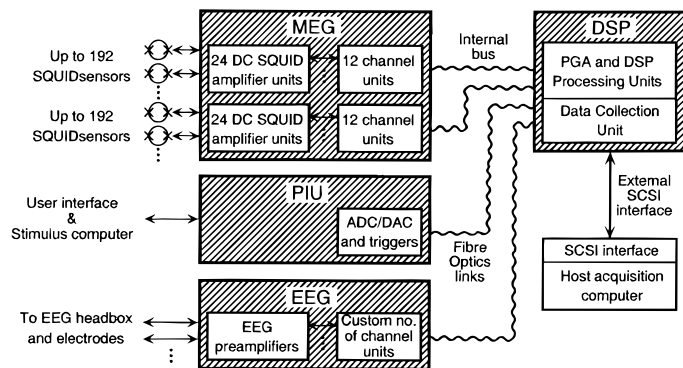


**FIG. 12.** Block diagram of the digital MEG/EEG electronics architecture, shown with two banks for up to 384 SQUID channels, and a custom number of EEG and ADC/DAC channels (8). dc SQUID amplifier units contain 8 channels per unit, the MEG "channel units" contain 16 channels per unit, and the EEG contain 32 channels per unit. PGA, programmable gate array; DSP, digital signal processor.

electronics architecture provides powerful processing capabilities, including real-time filtering, resampling, higher-order gradiometer synthesis (Section 2), display, and real-time execution of numerous other computationally intensive functions (such as covariance updates, cross-power updates, coherence calculations, spatial filtering). The electronics computational power can also be used for fast off-line processing of previously collected data.

MEG systems collect large quantities of data. To illustrate this point, consider, e.g., a system with 200 MEG channels, 64 EEG electrodes, 16 ADC/DAC channels and 4 miscellaneous channels. Each MEG and EEG channel data word is 4 bytes long, corresponding to 1056 bytes, and the ADC/DAC and miscellaneous channels are only 2 bytes long, corresponding to 40 bytes. Therefore, one sample of MEG system output is 1096 bytes long. If the sample rate was 4000 samples/s, then the data rate would be about 4.4 Mbyte/s. Consider specific experiments. For example an evoked field experiment (such as, e.g., AEF discussed before) may be collected with sample rate of 625 samples/s, 1.5-sec duration per trial, and a total of 100 trials, resulting in 103 Mbyte of data. Epilepsy monitoring at a sample rate of 2000 samples/s for 10 min would result in 1.3 Gbyte of data. If 10 to 15 patients were examined per day, the data volume would be 1 to 20 Gbyte per day.

#### 1.4. Cryogenics

The MEG sensing elements (SQUIDS, flux transformers, and their interconnections) are superconducting and must be maintained at low temperatures. Since all commercial MEG systems use low-temperature superconductors, they must be operated at liquid He temperatures. The He temperatures can be achieved either with cryocoolers or with a cryogenic bath in contact with the superconducting components. The cryocoolers are attractive because they eliminate the need for periodic refilling of the cryogenic container; however, they

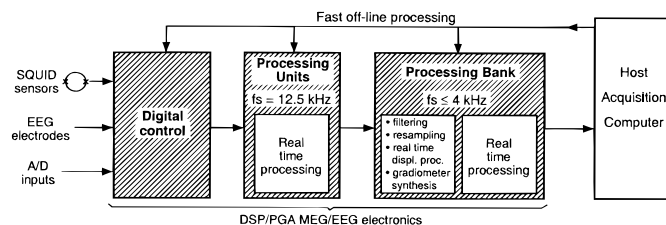


**FIG. 13.** Block diagram of the digital MEG system electronics (8) with capability for real-time preprocessing of MEG/EEG signals, real-time computation of numerically extensive tasks, and off-line capability as a fast processor.

contribute large magnetic interference and are not suitable for sensitive MEG instrumentation [EMI interference, vibrational noise, thermal fluctuations, and Johnson noise from metallic parts (44)]. The present commercial MEG systems rely on cooling by liquid He bath contained in a dewar. An example of how the components may be organized within the dewar is shown in Fig. 14a (8). The primary sensing flux transformers (radial gradiometers in this case) are positioned on He surface of the dewar helmet area. The reference system for the noise cancellation (Section 2) is positioned close to the primary sensors and the SQUIDs, with their shields located some distance from the references, all immersed in liquid He or cold He gas.

The dewar is a complex dynamic device that incorporates various forms of thermal insulation, heat conduction, and radiation shielding. An excellent review of the issues associated with dewar construction is presented in (44); only a qualitative description of the dewar operation is given here. A schematic diagram of the dewar inner structure is shown in Fig. 14b. Similar to the standard coffee thermos flasks, the He dewar is an evacuated double-walled vessel. Because the thermal differential between the environment and the He liquid is about  $300^{\circ}\text{C}$  (while for the coffee it may be only about  $50^{\circ}\text{C}$ ), thermal radiation losses (which are proportional to  $T^4$ ) are an important factor in the overall dewar heat budget. To protect the cryogen from the thermal radiation multiple layers of superinsulation (thin metallized mylar foil) are placed into the dewar vacuum space. Only two superinsulation layers are shown in Fig. 14b; however, in real dewars there may be several

tens of them. The cold gases from the evaporating He carry out energy that is captured in the dewar neck and conducted by heat shields back into the dewar vacuum space to help reduce the thermal gradient between the liquid He and the environment. Again, only one heat shield is shown in Fig. 14b, but several shields may be employed. The overall dewar design takes into consideration heat losses through radiation, conduction, and convection and minimizes them by using reflectivity, insulation, and energy extraction from the escaping He vapors. The dewar designs are highly efficient and the present commercial MEG systems consume liquid He at a rate of approximately 10 liters per day.

## 2. NOISE CANCELLATION

Noise at the output of MEG sensors is a combination of sensor white noise, brain noise, and environmental noise. Sensor noise can be minimized to acceptable levels by careful design of the SQUID and primary flux transformers, and brain noise (if it is considered noise and not signal) can be controlled or reduced by spatial filtering methods. Environmental noise is caused by various moving magnetic objects (cars, people, trains, etc.) or by electrical equipment (power lines, computers, various machinery, etc.). It is usually generated at larger distances from the MEG system and the magnetic interference magnitudes at urban locations or even at rural areas are many orders of magnitude larger

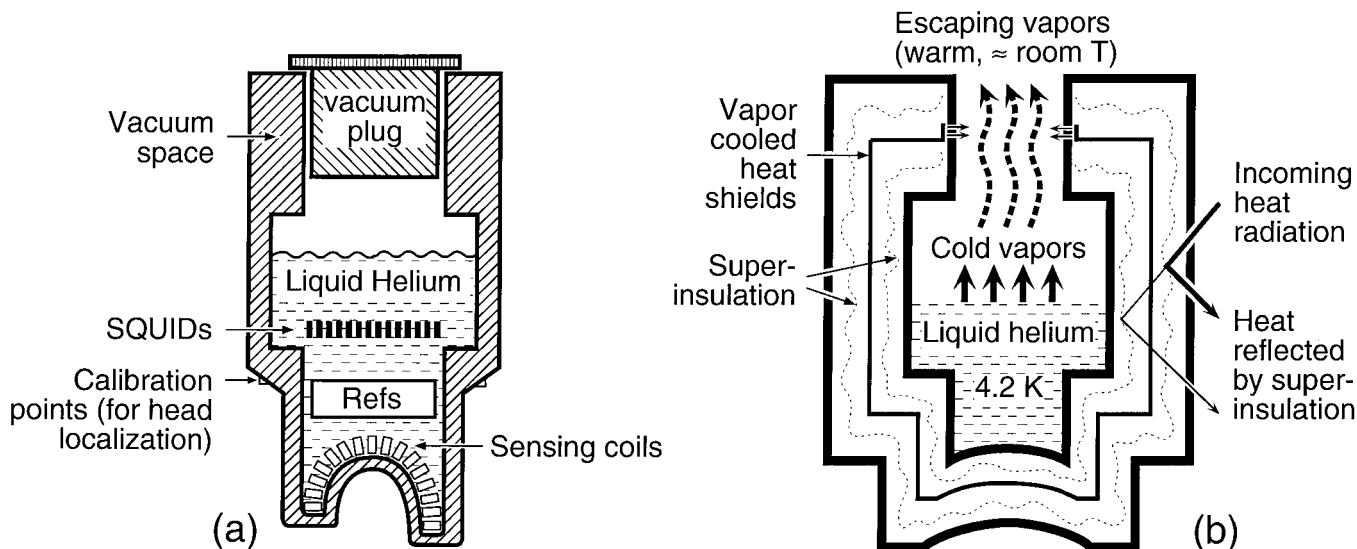


**FIG. 14.** Schematic diagram of cryogenics used for MEG. (a) Placement of various MEG components relative to the cryogenic dewar. (b) Principles of the dewar operation.

than the magnetic fields of the brain (42). It was suggested in Section 1.2 that the primary MEG sensors could be hardware gradiometers to help reduce the effect of the environmental noise. Even though such an approach is beneficial, it is not sufficient, and additional methods for environmental noise elimination have been the subject of intense study during MEG history. Environmental noise reduction by shielding, active noise compensation, synthetic gradiometers, adaptive methods, and spatial filtering is discussed or touched on in this section.

Enclosing the MEG system within a shielded enclosure (shielded room) is the most straightforward method for reduction of environmental noise. The simplest shielding can be accomplished by eddy currents using a thick layer of high-conductivity metal (54), but such shielding is not effective at low frequencies. Shielding using high-permeability materials provides low-frequency attenuation and is often also supplemented by eddy current shielding to enhance the higher-frequency attenuation. Typical shielded rooms for MEG exhibit a low-frequency shielding factor of 50 to 100 and the shielding factor increases in proportion to frequency above about 0.1 or 0.2 Hz (45). Shielded  $\mu$ -metal rooms with high attenuation in excess of about  $10^4$  at low frequencies have also been constructed, but they are expensive and are used mostly for experimental purposes [the recently constructed shielded room in Berlin is designed for low-frequency attenuation of  $\approx 3 \times 10^4$  without active shielding (46)]. The high levels of shielding can also be accomplished by superconducting shields, an example being the whole-body high-temperature superconducting  $\text{Bi}_2\text{Sr}_2\text{Ca}_1\text{Cu}_2\text{O}_x$  shield with attenuation approaching  $10^8$  (49).

The environmental magnetic noise of shielded or unshielded systems can be reduced by active noise compensation (50, 51). The active compensation consists of a reference detector of magnetic field, feedback electronics, and a set of compensating coils and is usually operated only at low frequencies. The sensors can be either SQUIDs, fluxgate magnetometers, or coils exposed to the environmental magnetic fields. If the sensors are located within a distance of about 1 m from the detection area, attenuation better than about 40 dB can be realized.

Hardware noise cancellation (shielding or active noise cancellation) is usually not sufficient and additional methods, implemented in software or firmware, are employed. These additional methods either use reference magnetic sensors (other than the primary MEG sensors) or operate directly on the MEG sensors (with or without the references). The references are typically a combination of SQUID magnetometers and gradiometers and the noise is cancelled by synthesizing either

higher-order gradiometers or adaptive systems. If references are not used, spatial filtering methods (signal space projection or beamformers) are employed. Spatial filtering is often a part of the signal interpretation and is discussed in more detail in Section 4. The discussion in this section concentrates on noise cancellation by using references.

When canceling noise using references, a linear combination of the reference outputs is subtracted from the MEG primary sensor output and the coefficients of the linear combination are selected to reduce environmental noise. The subtraction coefficients may be chosen either to mimic a higher-order gradiometer component or on the basis of some other requirement (e.g., minimum noise). The advantage of synthesizing higher-order gradiometers is that their coefficients are truly universal; they can be factory predetermined and are independent of the noise character or dewar orientation (43). In contrast, the coefficients determined by adaptation for minimum noise are not universal because they depend on the noise character and dewar orientation (48). Thus even though the adaptation coefficients can provide lower noise than the synthetic gradiometer coefficients, the frequent need for readaptation for every dewar orientation or change of the noise character makes them less desirable than the gradiometer coefficients. However, in MEG systems equipped with sufficient number of references, the switch between the gradiometer or adaptive coefficients is a software operation and both methods can be simultaneously available (43).

Since the synthetic gradiometers provide stable and excellent noise cancellation which is additive to the attenuation of the shielded rooms, their synthesis is discussed in greater detail. The principle of synthetic gradiometer operation is similar for all gradiometer orders, and the method is illustrated on simple examples of first- and second-order gradiometers (42). First, consider a first-order gradiometer synthesized from a magnetometer primary sensor and a three-component vector magnetometer reference, as in Fig. 15a. The primary magnetometer detects the magnetic field component parallel to its coil normal,  $\mathbf{p}$  (unit vector). If the magnetometer gain was  $\alpha_p$  and the environmental field was  $\mathbf{B}$ , the primary magnetometer would detect  $m_p = \alpha_p(\mathbf{p}\mathbf{B})$ . The three reference magnetometers are orthogonal and have identical gains  $\alpha_r$  and their outputs will be  $r_k = \alpha_r B_k$ ,  $k = 1, 2, 3$ , where  $B_k$  are components of  $\mathbf{B}$ . The components  $r_k$  form a vector of the reference magnetometer output,  $\mathbf{r}$ . Then, by expanding the magnetic field into a Taylor series about the origin, defining gradiometer baseline  $\mathbf{b}$  as a vector connecting the primary magnetometer center and the reference center, and projecting the reference output to the direction  $\mathbf{p}$ ,

the synthetic first-order gradiometer,  $g^{(1)}$ , can be derived as

$$g^{(1)} = m_p - \frac{\alpha_p}{\alpha_r} (\mathbf{pr}) \approx \alpha_p \mathbf{p} \mathbf{G} \mathbf{b}, \quad [3]$$

where  $\mathbf{G}$  is the first gradient tensor at the coordinate origin. Note that in this and all subsequent derivations, the gradiometer output is expressed as field; i.e., the gradient tensor components are multiplied by the relevant gradiometer baselines. Equation [3] states that the synthetic first-order gradiometer is a projection of the first gradient tensor to the primary magnetometer orientation,  $\mathbf{p}$ , and the baseline,  $\mathbf{b}$ . If  $\mathbf{p}$  and  $\mathbf{b}$  orientations are general, the synthetic gradiometer in Eq. [3] consists of a linear combination of the first gradient tensor components.

Synthesis of a second-order gradiometer is similar (see Fig. 15b). Assume that there are two first-order gradiometers with parallel baselines  $\mathbf{b}$  and  $\mathbf{b}'$ , and parallel coil orientation unit vectors  $\mathbf{p}$  and  $\mathbf{p}'$ , and the output of each gradiometer is given by Eq. [3] as  $g^{(1)}$  and  $g^{(1)'}$ . The second-order gradiometer baseline,  $\mathbf{q}$ , connects the two gradiometer centers. The second-order gradiometer,  $g^{(2)}$ , is synthesized similar to the first-order gradiometer by scaling the gains and baselines and subtracting first-order gradiometer outputs (42),

$$g^{(2)} = g^{(1)} - \frac{\alpha_g b}{\alpha_{g'} b'} g^{(1)'} \approx \alpha_g \mathbf{p} \mathbf{G}^{(2)} \mathbf{q} \mathbf{b}, \quad [4]$$

where  $\alpha_g$  is the first-order gradiometer gain and  $\mathbf{G}^{(2)}$  is the second gradient tensor at the coordinate origin.

Equation [4] shows that the synthetic second-order gradiometer is a projection of the second gradient tensor into the coil orientation vector  $\mathbf{p}$  and baseline vectors  $\mathbf{q}$  and  $\mathbf{b}$ . Again, if  $\mathbf{p}$ ,  $\mathbf{q}$ , and  $\mathbf{b}$  orientations are general, the synthetic second-order gradiometer output will be a linear combination of the second gradient tensor components.

The above discussion illustrates the approach to higher-order gradiometer synthesis. The procedure can be generalized and it can be shown that second- or third-order gradiometers can be synthesized from magnetometers, or first-order gradiometers, or their combinations.

The synthetic higher-order gradiometers substantially reduce the environmental noise and yet, from the MEG signal point of view, they behave nearly like the primary sensors on which they are based. Specifically, the synthetic gradiometers do not increase the white noise levels (because the references are designed with higher gain than the primary sensors) and they do not substantially reduce the MEG signal; in fact they can slightly increase it or reduce it, depending on the exact configuration of the MEG sources and references (52). This is illustrated in Fig. 16 where an auditory evoked field for one channel is displayed for a primary hardware first-order gradiometer and a synthetic third-order gradiometer based on the same primary sensor. In this example the synthetic third-order gradiometer signal amplitude is slightly larger than that of the hardware first-order gradiometer.

The low noise and small effect on the MEG signals for synthetic gradiometers are very different from what is usually observed for hardware gradiometers of the

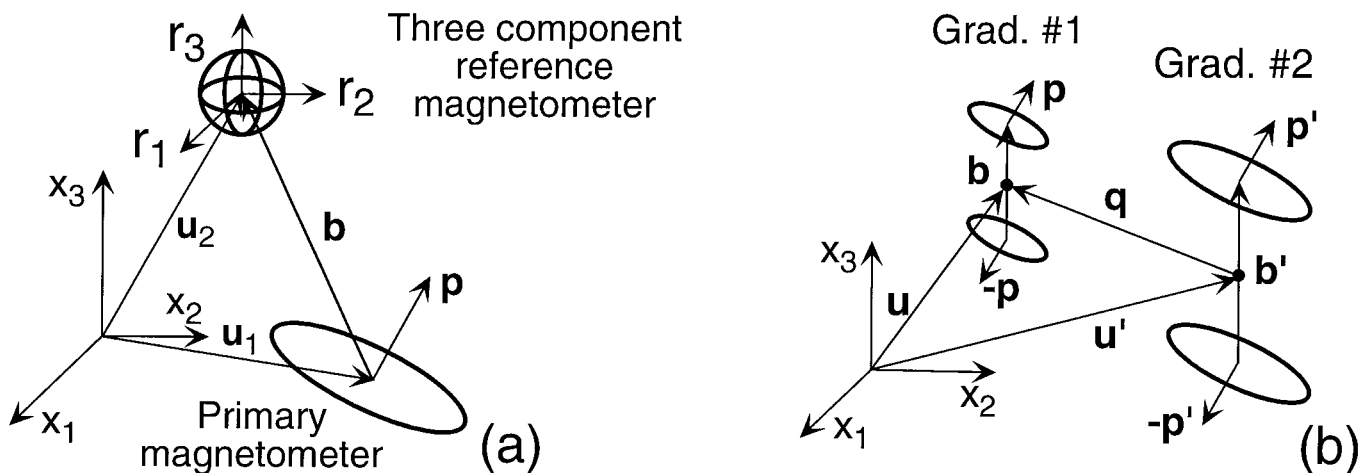


**FIG. 15.** Illustration of gradiometer synthesis. (a) Synthesis of a first-order gradiometer from a primary magnetometer sensor and a vector magnetometer reference. (b) Synthesis of a second-order gradiometer from two hardware first-order gradiometers.

same order and approximate dimensions. Hardware higher-order gradiometers provide large inductive loading on the SQUID sensor and reduce overall sensitivity (42), while synthetic higher-order gradiometer sensitivity is typically indistinguishable from that of the primary sensor. Similarly, hardware higher-order gradiometers are known to strongly reduce MEG signals,

while the effect of synthetic gradiometers on MEG signal is small and they can either increase or reduce it (52) (Fig. 16).

Environmental noise reduction by the synthetic gradiometers is illustrated in Fig. 17a for a 151-channel MEG system operated within a shielded room. The gray traces show noise spectra of all channels, the black lines overlying the gray show rms noise computed over all channels. Note that the spectral lines at about 1.8 and 7 Hz are completely eliminated by synthetic third-order gradiometers. At low frequencies, synthetic third-order gradiometers reduce the primary first-order hardware gradiometer sensor noise by about two orders of magnitude and reduce magnetometer noise by about four orders of magnitude (43). The effect of a shielded room is additive to the synthetic gradiometer noise reduction. If shielded room attenuation at low frequencies were about a factor of 70, the combined shielded room and synthetic third-order gradiometer attenuation of the environmental noise would be about  $7 \times 10^5$ .

Synthetic gradiometers also dramatically reduce MEG system sensitivity to vibrational noise. This is illustrated in Fig. 17b, where measurement during patient head motion is shown. Head motion is clearly

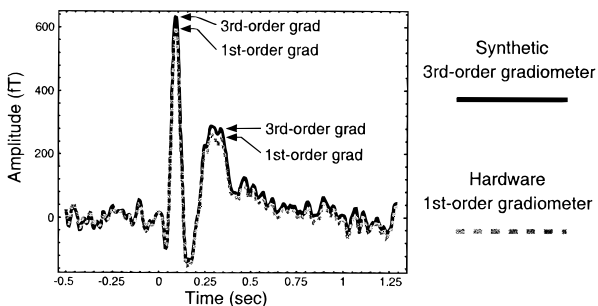


**FIG. 16.** Synthetic higher-order gradiometers do not reduce signal. Example of auditory evoked fields measured with hardware first-order gradiometer and synthetic third-order gradiometer, 100 averages, measured in shielded room. In this example, the synthetic third-order gradiometer signal magnitude is larger than that of the first-order hardware gradiometer.

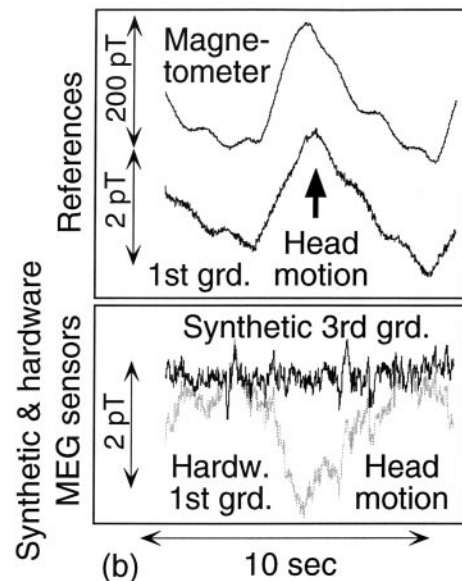
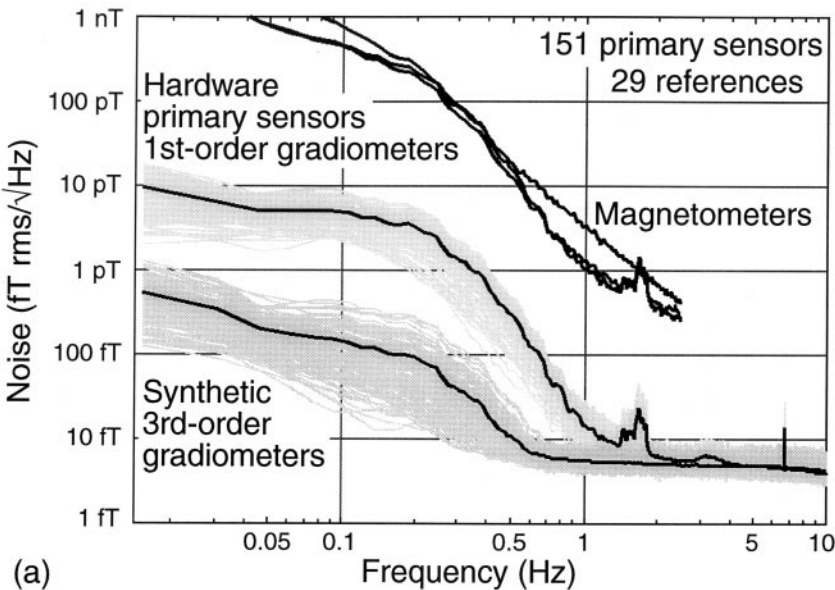


**FIG. 17.** Examples of synthetic gradiometer performance. (a) Noise spectra of magnetometers, hardware first-order gradiometer primary sensors, and synthetic third-order gradiometers for all channels of 151-channel MEG system with 29 references, operated within a shielded room (43) (b) Illustration of synthetic third-order gradiometer immunity to vibrations. The patient head motion artifacts are completely eliminated by the synthetic third-order gradiometer.

visible in the references and the primary first-order hardware gradiometer sensor, but it is completely eliminated by the synthetic third-order gradiometer.

### 3. EEG

Electric potentials (EEG) and magnetic fields (MEG) are related because they both detect the same current generators. While radial magnetic fields are generated mostly by the intracellular current, the EEG measures volume currents. Magnetic field maps and electric field patterns on the surface of the scalp are orthogonal (Fig. 18a), and an experimental demonstration of EEG/MEG orthogonality for mechanical stimulation of the right index finger can be found in (53). The EEG and MEG must be measured simultaneously to take advantage of the complementary information. EEG electrodes and all their connections must be nonmagnetic to avoid creation of MEG artifacts. A view of a subject with EEG electrodes attached is shown in Fig. 18b.

### 4. DATA INTERPRETATION

Much of the signal analysis used for MEG has been inherited from EEG applications. However, MEG is more commonly used for quantitative assessment of brain activity, especially for source localization. Electrophysiological activity is characterized by a primary ionic current, flowing within cell bodies (the "source current"), and a volume or return current, flowing in the extracellular space. Biomagnetic sensors are coupled mainly to the primary current sources; biomagnetic

measurements can be configured so that there is little contribution from volume currents.<sup>1</sup> By contrast, bioelectric potential measures volume currents only. As such, source current determination from EEG measurements also requires accurate knowledge of the conductivity distribution. Since MEG measurements have only weak dependence on tissue conductivity, primary current sources are readily localized, without having knowledge of tissue conductivity or its boundaries.

The overall goals of MEG analysis are twofold: first, enhancement of signal-to-noise ratio of electrophysiological signals so that they may be readily identified and classified; second, determination of where the signals originate. In this section, we outline only the quantitative aspects of MEG analysis, and focus on the functional imaging method, synthetic aperture magnetometry (SAM). Quantitative MEG implies derivation of objective indices of the signals being measured. The following categories are examples of quantitative techniques:

1. *Time-amplitude analysis*: Automated characterization of waveforms, including epileptic spike identification, appearance or suppression of brain rhythms such as  $\alpha$  (8–13 Hz) and  $\beta$  (15–30 Hz), and identification of hemispheric asymmetries.

2. *Frequency-amplitude analysis*: Estimation of MEG frequency content using Fourier transform or maximum entropy methods.

3. *Coherence analysis*: Estimation of correlation of

<sup>1</sup> The normal component of the magnetic field at the surface of a conducting body will have the minimum contribution of volume currents.

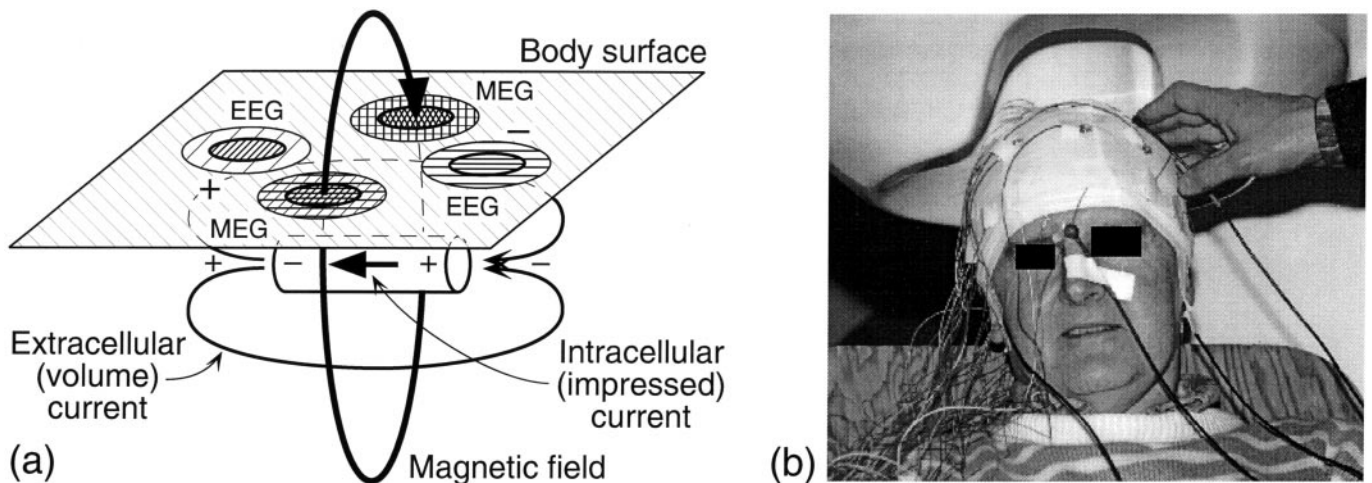


**FIG. 18.** EEG. (a) Orthogonal relationship between EEG and MEG signals. (b) A subject with attached EEG electrodes before head insertion into the MEG helmet.

an MEG signal channel with other channels (MEG, EEG, or measured events).

4. *Averaged evoked response*: The averaged MEG signal—synchronous with an external stimulus or voluntary motor event.

5. *Topographic mapping of signal and power*: Distribution of band-limited signal power, mapped to the sensor surface.

6. *Forward and inverse solutions*: Computation of fields from a current source model, with adjustment of model parameters for best fit to the observed field pattern. Models include single and multiple equivalent current dipoles (ECDs) (55) and continuous current distributions (minimum norm) (56).

7. *Spatial filters*: Weighted linear combinations of measurements that separate signals by their spatial origin.

8. *Three-dimensional mapping of source power*: Estimation of source power or a statistical derivative. Not to be confused with inverse solution. Methods include SAM (57), linear beamforming (58), and MUSIC (59).

Historically, MEG data analysis has focused on the ubiquitous averaged evoked response paradigm. The underlying assumption of this method is that the activation of some areas of the brain is time-locked to external events, either to a stimulus or to a motor outflow. Averaging the MEG or EEG signals enhances the signal-to-noise ratio of the time-locked fraction of brain activity. This, in turn, permits reproducible quantitative measures of that specific activity. For example, a map of the averaged evoked response to transient tone bursts reveals a characteristic two-dipole pattern at 100-ms latency relative to stimulus onset (see Fig. 19b). Unfortunately only a small portion of the brain is accessible to this method. Primary sensory and motor areas activate synchronously with external events. However, regions serving higher cognitive functions have much more variable latency. The averaged signals of time-variable events cannot faithfully reproduce the character of their sources.

The advent of large MEG sensor arrays with whole-head coverage has altered the strategy of signal analyses. Let us consider the averaged evoked response paradigm: The increase in channel count has decreased the time required to map an evoked response, but has not yielded additional information. In fact, the evoked response mapped by a large whole-head array will be identical to that detected by serial multiple placement and measurement by a single-channel MEG sensor at the same sites.<sup>2</sup>

<sup>2</sup> Within the reproducibility of the averaged evoked response, and assuming that the subject's state of attention to the stimulus is maintained.

Signal averaging does not make use of the information available from large MEG sensor arrays. The unaveraged MEG signals exhibit spatial and temporal correlation. This correlation may be used to advantage in improved separation of source signals from the noise and the localization of activity.

The three-dimensional source estimation method will be illustrated using SAM. It is a robust method, providing excellent spatial resolution, and is suitable for analysis of nonaveraged MEG signals. SAM uses the spatial and temporal correlation of a MEG array. Consider an array of  $M$  sensors, with instantaneous measurements  $\mathbf{m} = \{m_1, m_2, \dots, m_M\}$ . Each sensor responds to time-varying bioelectric currents  $\mathbf{J}(\mathbf{r})$  within the brain. The response of each sensor to the current is given by the volume integral,

$$m_i(t) = \int_{\Omega} \mathbf{J}(\mathbf{r}) \mathbf{G}_i(\mathbf{r}) dV + n_i(t) \quad [5]$$

where  $\mathbf{G}_i(\mathbf{r})$  is Green's function<sup>3</sup> describing that sensor's response to current at each coordinate  $\mathbf{r}$ . The measurement may also have added instrumental noise  $n_i(t)$ . To use the entire sensor array to estimate source activity  $\hat{S}_{\theta}(t)$  at voxel  $\theta$  within the head, let us form a weighted linear combination of all measurements:

$$\hat{S}_{\theta}(t) = \mathbf{W}_{\theta}^T \mathbf{m}(t). \quad [6]$$

The coefficients  $\mathbf{W}_{\theta}$  are to be selected so that they emphasize activity at  $\theta$ , and attenuate signals from all other locations, including environmental magnetic interference. The optimal coefficients may be found by minimizing the total power over time, which can be expressed as  $\mathbf{W}_{\theta}^T \mathbf{R} \mathbf{W}_{\theta}$ , where  $\mathbf{R}$  is the  $M \times M$  correlation matrix of the measurements. The SQUID sensors used for MEG have an unknown dc baseline, depending on the nearest flux quantum for which the flux-locked loop acquired lock. The baseline offset occupies one degree of freedom in the correlation matrix, and is not a problem, provided that a sufficient number of time samples have been integrated into the correlation matrix. To eliminate this bias, one can substitute the covariance matrix  $\mathbf{C}$  for correlation matrix  $\mathbf{R}$ , giving

$$\mathbf{W}_{\theta} = \mathbf{C}^{-1} \mathbf{B}_{\theta} [\mathbf{B}_{\theta}^T \mathbf{C}^{-1} \mathbf{B}_{\theta}]^{-1}. \quad [7]$$

An estimate of the mean-squared source power at  $\theta$  can, in fact, be determined without computing the weighting coefficients as

<sup>3</sup> In the electrophysiology literature, Green's function is often referred to as the "lead field."

$$\hat{Q}_\theta^2 = [\mathbf{B}_\theta^T \mathbf{C}^{-1} \mathbf{B}_\theta]^{-1}. \quad [8]$$

In principle, an image of the source power distribution in three dimensions could be generated by applying the latter equation to coordinates on some grid of points in the head. This is referred to as “source scanning.”<sup>4</sup> However, the signal-to-noise ratio of the source estimate declines with depth and distance from the sensors. Furthermore, due to the limited spatial selectivity of the process, unwanted source power may “leak” into the source estimate. Near the center of the head, the total noise power may be so large as to obscure source activity. One can readily compensate for the noise by a normalization process.

To implement such normalization, let us consider the instrumental noise variance of an array of sensors:

$$\Sigma = \begin{bmatrix} \nu_1^2 & & & 0 \\ & \nu_2^2 & & \\ & & & 0 \\ 0 & & & \nu_M^2 \end{bmatrix}. \quad [9]$$

Assuming that all sensors have equal noise, the noise matrix can also be represented by  $\Sigma = \bar{\nu}^2 \mathbf{I}$ . The contri-

<sup>4</sup> One distinguishes source scanning from inverse solutions in that the latter involves fitting a model to the observed field, by adjusting the parameters of the model so as to minimize a distance function such as  $\chi^2$ . Scanning methods (including the MUSIC algorithm) are not inverse solutions for source.

bution of sensor noise to the power is the weighted sensor noise for that voxel:

$$\hat{\nu}_\theta^2 = \mathbf{W}_\theta^T \Sigma \mathbf{W}_\theta. \quad [10]$$

The normalized voxel value becomes

$$\mathcal{Z}_\theta^2 = \frac{\hat{Q}_\theta^2}{\hat{\nu}_\theta^2}. \quad [11]$$

The symbol  $\mathcal{Z}$  (pronounced pseudo- $Z$ ) denotes the analogy of this quantity to the classic  $Z$  deviate of descriptive statistics.

We illustrate this analysis with an example of source activity mapping, using  $\mathcal{Z}$ , in Fig. 20a; the SAM  $\mathcal{Z}$  image is shown superimposed on the MRI image. A 143-channel whole-cortex MEG (CTF Systems Inc. [8]) was used to measure epileptic spike activity in an 8-year-old patient. A total of 100 s of MEG signal (as ten 10.0-s epochs) was acquired at a sample rate of 625 Hz.<sup>5</sup> The signal was band-limited from 30 to 55 Hz, prior to SAM analysis, to exclude the contribution of the dominant  $\alpha$ - and  $\beta$ -band brain rhythms to the image. The regions of interictal spike generation are characterized by high-frequency activity. These appear as bright regions of activity in the SAM  $\mathcal{Z}$  image.

<sup>5</sup> Data were collected in the open environment, without magnetic shielding, using third-order synthetic gradiometer sensors.

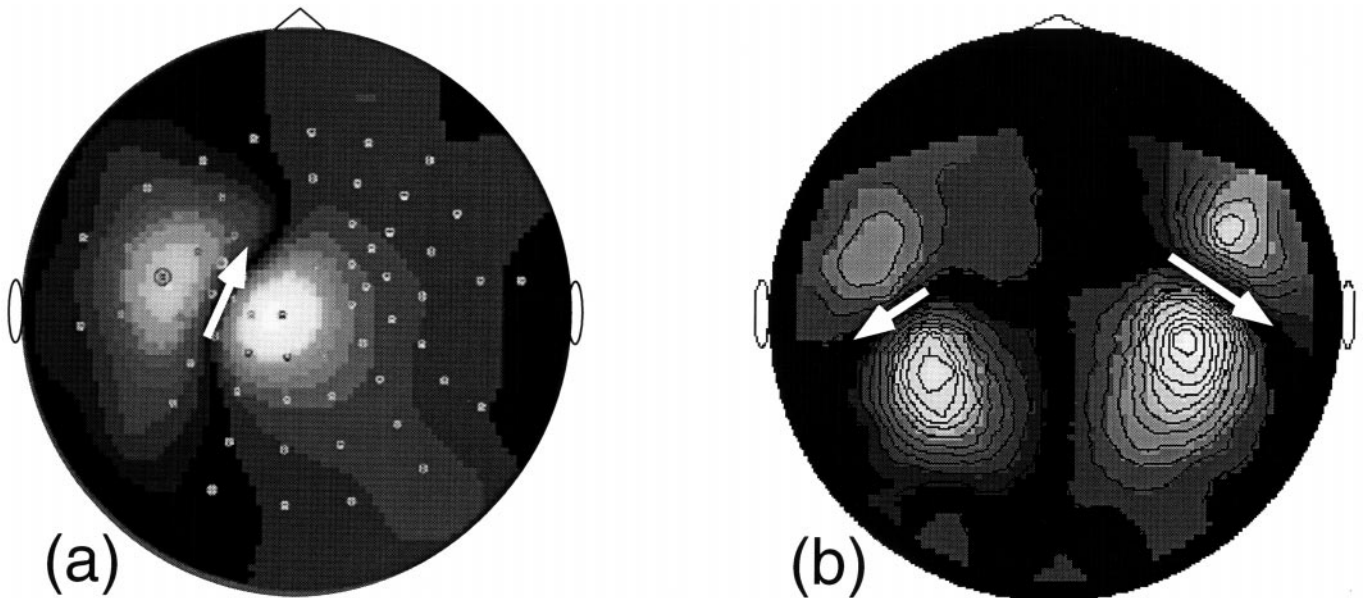


**FIG. 19.** Example of averaged event-related MEG data analysis. The field maps can be interpreted by discrete ECDs, shown by white arrows. (a) One-dipole map corresponding to somatosensory (SEF) stimulation of the median nerve. (b) Two-dipole field map corresponding to auditory evoked fields.

The analogous true  $Z$ -deviate image (ratio of averaged source power to its standard deviation, for multiple epochs) also provides normalization for the increase in image power with depth. This is shown in Fig. 20b. However, the true  $Z$  deviate does not convey source information in the same manner as its pseudo- $Z$  kin. Epileptic spike events occur at random throughout the MEG recording. Each of the ten 10.0-s epochs contained different rates of spike activity. Hence, the  $Z$ -deviate score appears lowest (dark, in the image) at the spiking loci.

Source activity related to performance of a task is

most easily identified by subtraction of the common-mode brain activity. To accomplish this, MEG data are collected during both task performance, active (a), and background activity, control (c). The simple power difference,

$$\Delta \hat{Q}_\theta^2 = {}^{(a)}\hat{Q}_\theta^2 - {}^{(c)}\hat{Q}_\theta^2, \quad [12]$$

suffers from the same noise degradation as does the single-state SAM source image. Once more, we apply the noise normalization to each voxel to compute its pseudo- $T$  value:

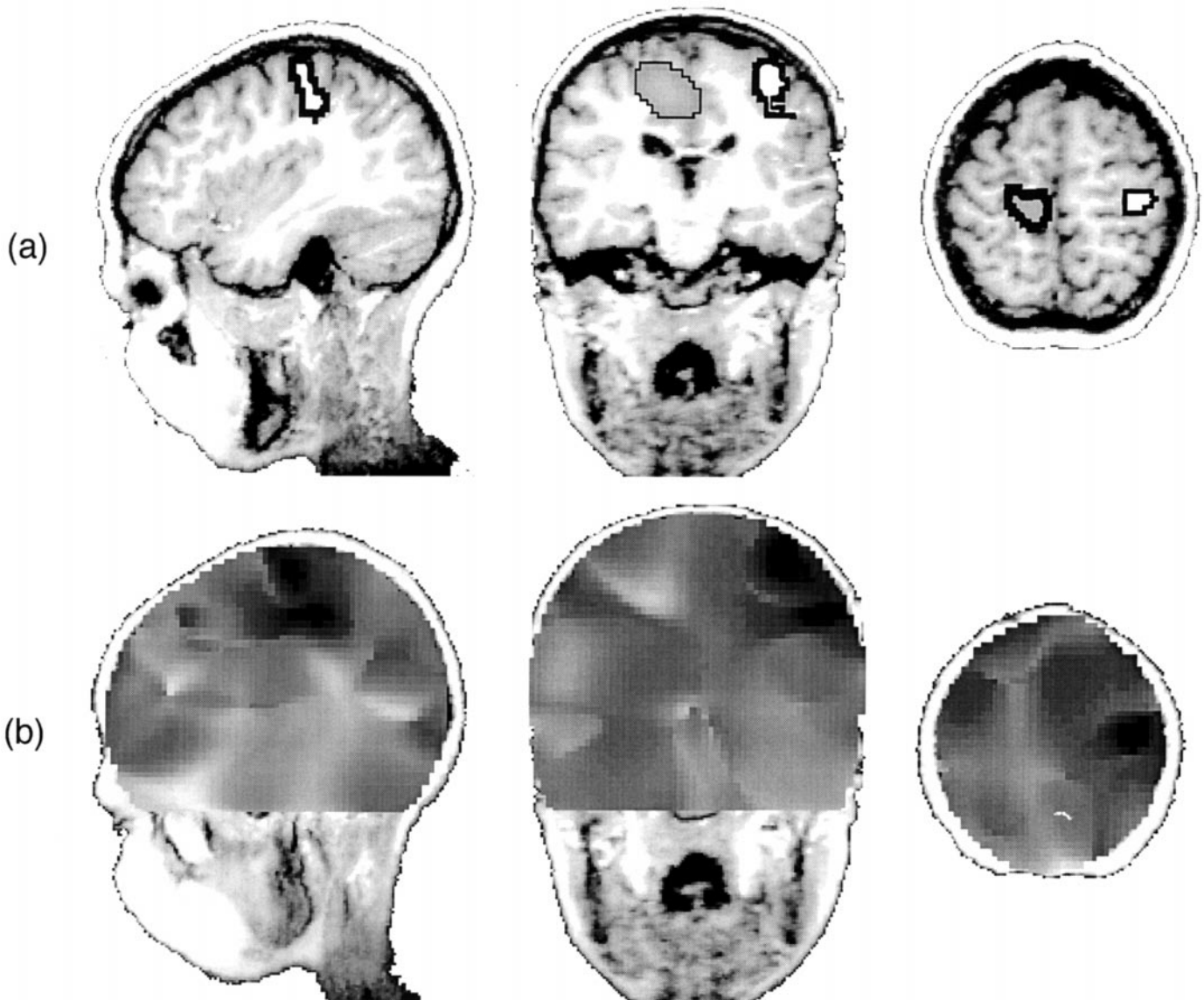


**FIG. 20.** SAM images of MEG recording of interictal spike activity, fused to the patient's MRI. The three orthogonal views intersect at a common point in the head. Activity is mapped for the 30 to 55-Hz band. (a) The interictal spike source activity shown by outline as SAM pseudo- $Z$  value (peak value  $Z_{\max} = 10.4$ ). (b) The same MEG data are also mapped using the  $Z$  deviate. The spike loci appear dark (marked by white dot), because they have high statistical variability.

$$\mathcal{F}_\theta = \frac{^{(a)}\hat{Q}_\theta^2 - ^{(c)}\hat{Q}_\theta^2}{^{(a)}\hat{\nu}_\theta^2 + ^{(c)}\hat{\nu}_\theta^2}. \quad [13]$$

To illustrate this, a simple voluntary motor study was performed. A subject was directed by voice command to squeeze a sponge with one hand for 10 s and relax the hand for 10 s. Ten trials of MEG data were acquired, with each trial consisting of squeezing and then relaxing. Data were collected at 625-Hz sample rate in the open environment, using a 143-channel whole-cortex MEG [CTF Systems Inc. (8)] with synthetic third-order gradiometer sensors. A pseudo- $T$  SAM image was mapped for  $\beta$ -band (15–30 Hz) activity. This is shown in Fig. 21a. Voluntary motor movement is accompanied by event-related suppression of  $\beta$ -band activity. As can be seen in these images, the source of the suppression

for one-handed squeezing is localized to the hand region of the central sulcus.

The true  $T$  statistic can be computed from multiple-trial SAM images of active and control activity,

$$T_\theta = \frac{^{(a)}\hat{Q}_\theta^2 - ^{(c)}\hat{Q}_\theta^2}{\sqrt{\sigma^2/N}}, \quad [14]$$

where  $\sigma^2$  is the pooled variance and  $N$  the total number of instances of both the active and control events. A SAM source power image is generated for each instance of active and control activity. The mean active, mean control, and their pooled standard error are used to compute Student's  $T$  value for each voxel. Like the pseudo- $T$  value this procedure compensates for the increase in noise power with depth in the head. The statistical probability of each voxel can also be computed

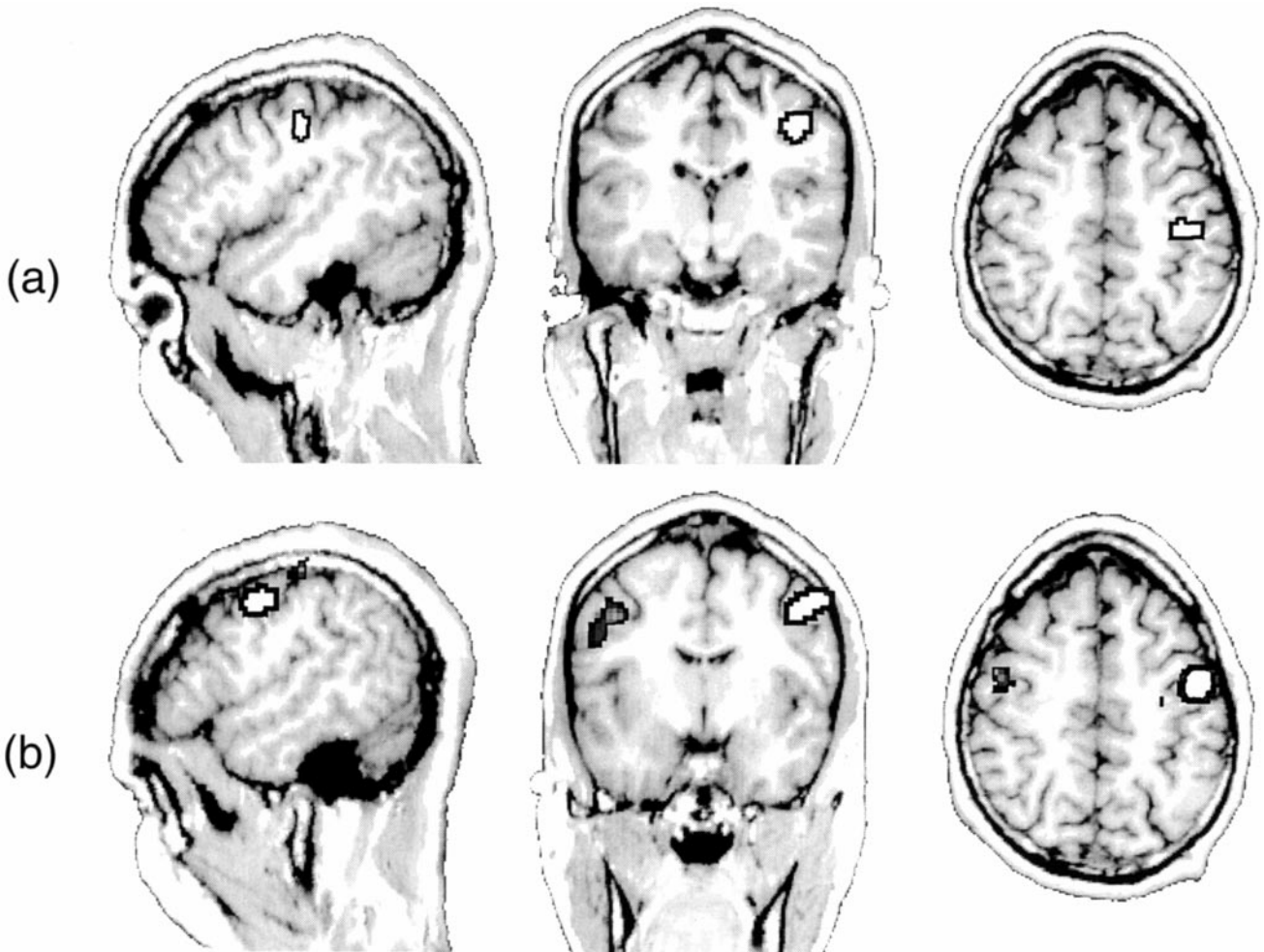


**FIG. 21.** SAM images of MEG recording during voluntary hand motor activity (squeezing). Ten trials, each with 10.0 s of squeezing and 10.0 s of relaxation, were recorded. (a) The pseudo- $T$  image ( $\mathcal{F}_{\max} = 6.5$ ) shows a focal region of  $\beta$ -band suppression in motor cortex in the hemisphere opposite the hand that was squeezing. (b) Student's  $F$  statistic image ( $T_{\max} = 10.4$ ) of the same data reveals a weaker ipsilateral suppression, in addition to the contralateral site found with pseudo- $T$ .

from the true  $T$  statistic. A  $T$  image of the motor MEG data is shown in Fig. 21a. The peak  $T$  value in the image is 10.39 (19 degrees of freedom). Thus, the regions of activation are highly significant.

Student's  $T$  images show activity in similar locations to the pseudo- $T$  images. This differs from the SAM images of epileptic activity shown in Fig. 20. It indicates that the suppression of  $\beta$ -band activity is reproducibly present during each of the active-state (squeezing) trials, since the variance over trials is small. This contrasts with the epileptic activity for which interictal spikes occurred sporadically, resulting in large variance and therefore low  $Z$ -deviate scores.

## 5. CONCLUSIONS

The rationale for using magnetoencephalography to study the brain is twofold: First, the physics of magnetic measurement permit three-dimensional localization of

current sources. Second, the changes in ionic source currents can be studied on a time scale of less than 1 ms. Thus, MEG can be used for functional neuroimaging of events that are not accessible either to functional MRI or to nuclear imaging methods. Let us retrace the fundamentals of MEG from its origin as electrophysiological ionic source currents within the brain to the presentation of analyzed results.

We have shown that the magnetic field of the brain is many orders of magnitude smaller than fluctuations of the environmental magnetic field. This implies the need for highly sensitive sensors as well as sophisticated noise cancellation techniques.

At present, the most sensitive magnetic detectors are based on the SQUID (superconducting quantum interference device). Other classes of magnetic detectors are too noisy to characterize the spontaneous (unaveraged) MEG or have poor frequency response. Modern SQUID-based MEG sensors can achieve a noise density of a few femtotesla per root hertz, in a bandwidth from dc

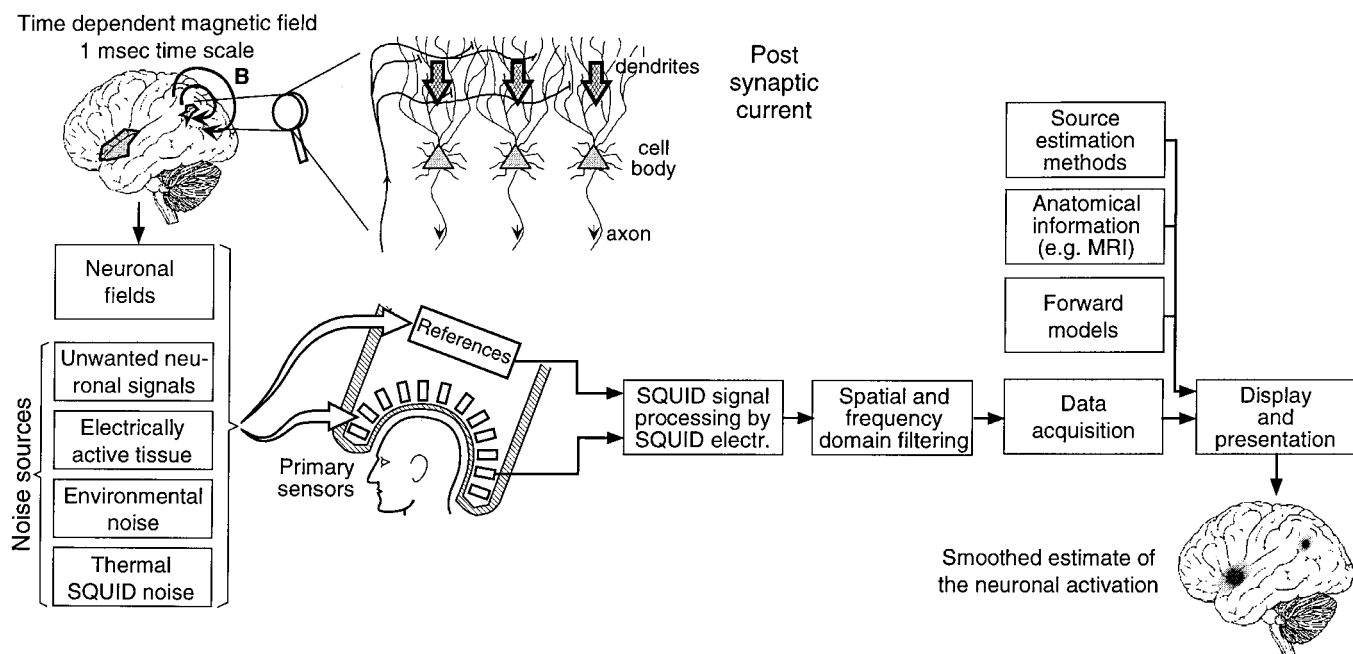


**FIG. 22.** Overview of the MEG signal processing chain. The MEG signals originate in the brain neurons. Activation of the individual neurons is not detectable and only the collective activations of large number of neurons are detected by the primary SQUID sensors (Section 1). In addition to the brain signals, the SQUID sensors are also exposed to the environmental and body noise. To eliminate the environmental noise, reference sensors, positioned farther from the scalp, are often used. The reference signals are subtracted from the primary sensor outputs to reduce the detected noise; the process can be understood as spatial high pass filtering. The SQUID design and optimization of the primary sensor flux transformers were discussed in Section 2 and the noise cancellation was outlined in Section 3. After the noise reduction, the detected signals are processed to the required bandwidth and the data are acquired. The data processing and acquisition by the digital SQUID electronics were discussed in Section 2.3. The acquired data represent magnetic field on the scalp surface and must be interpreted to yield information about the brain sources. This process requires additional information about the anatomical structure, forward models of the brain sources, and methods for source estimation from the measured fields. These steps were discussed in Section 5. The brain magnetic fields were generated by a specific distribution of the neuronal currents as shown in the upper left side of this figure. After the measurement, processing, and interpretation, a smoothed estimate of the neuronal activity is obtained, as shown in the lower right side of the figure.

to several kilohertz. The principles of SQUID operation have been outlined, showing how SQUIDS are coupled to the brain magnetic field using superconducting flux transformers. Conditioning electronics are required to transform the quantum periodic signals of the SQUIDS into a linear representation of the magnetic field. The periodic nature of the SQUID response allows recordings with a dynamic range of 192 dB (32 bits) or greater. SQUID electronics is partially digital and is intimately coupled to the fast digital signal processing using DSPs and PGAs to provide efficient preprocessing of the MEG data before acquisition and analysis by the collection computers. A typical MEG system may have several hundred primary sensors disposed about the head and can generate data volumes of up to several tens of gigabytes per day.

For an instrument to measure MEG in the open environment (without a magnetically shielded room), it must possess sensors and electronics capable of handling a very large dynamic range (approaching 30 bits). Furthermore, the impulse response of all primary sensors and their reference channels must be accurately matched and have low distortion, to obtain effective environmental noise cancellation and for accurate data analysis.

Interpretation of MEG data is complicated by the fact that the solution for the three-dimensional source current distribution in the brain from any array of sensors outside the head is nonunique. Useful source estimates can be obtained only after incorporation of constraints, prior assumptions, and mathematical simplifications. The spatial filtering approach offers an alternative to inverse solution by isolating signals from different parts of the brain.

We now summarize in Fig. 22 the steps in functional brain imaging by MEG, leading from the electrophysiological source currents within the brain to interpretation of the resultant magnetic signals. Brain activity is associated with electrochemical events that result in primary and secondary ionic currents. These currents give rise to magnetic fields which, together with the environmental magnetic noise, are detected by superconducting flux transformers. The environmental noise is attenuated using reference sensors that are remote from the head, and the data acquisition in the desired bandwidth is performed. The acquired magnetic field is combined with anatomical information, forward models, and analysis procedures for source estimation. Because the sensors cannot detect the activation of individual neurons (due to the spatial and field amplitude conditions) and because the inversion problem is non-unique, the procedure yields a smoothed "estimate" of the original neuronal activation.

## REFERENCES

- Berger, H. (1929) *Arch. Psychiat. Nervenkr.* **7**, 527–570.
- Cohen, D. (1968) *Science* **161**, 784–786.
- Jaklevic, R., Lambe, R. C., Silver, A. H., and Mercereau, J. E. (1964) *Phys. Rev. Lett.* **12**, 159–160.
- Zimmerman, J. E., and Silver, A. H. (1964) *Phys. Lett.* **10**, 47–48.
- Josephson, B. D. (1962) *Phys. Lett.* **1**, 251–253.
- Cohen, D. (1972) *Science* **175**, 664–666.
- Wikswow, J. P., Jr. (1995) *IEEE Trans. Appl. Supercond.* **5**, 74–120.
- CTF Systems Inc., 15-1750 McLean Ave, Port Coquitlam, BC, Canada.
- 4D Neuroimaging, 9727 Pacific Heights Blvd., San Diego, CA 92121-3719.
- Yokogawa Electric Corp., MEG Business Center, 2-9-32 Nakacho, Musashino-city, Tokyo, 180-8750, Japan.
- Nakaya, Y., and Mori, H. (1992) *Clin. Phys. Physiol. Meas.* **13**, 191–229.
- Carpenter, M. B. (1985) *Core Text of Neuroanatomy*, Williams & Wilkins, Baltimore London.
- Partridge, L. D., and Partridge, L. D. (1993) *The Nervous System, Its Function and Its Interaction with the World*, A Bradford Book, MIT Press, Cambridge.
- Sarvas, J. (1987) *Phys. Med. Biol.* **32**, 11–22.
- Wikswow, J. P., Jr. (1989) in *Advances in Biomagnetism* (Williamson, S. J., et al., Eds.), Plenum, pp.1–18, New York/London.
- Williamson, S. J., and Kaufman, L. (1981) *J. Magn. Magn. Mater.* **22**, 129–201.
- Okada, Y. C., Papuashvili, N., and Xu, C. (2000) in *Biomag96: Advances in Biomagnetism Research* (Aine, C., et al., Eds.), Springer-Verlag, Berlin, in press.
- Nakasato, N., Fujita, S., Seki, K., Kawamura, T., Matani, A., Tamura, I., Fujiwara, S., and Yoshimoto, T. (1995) *Electroencephalogr. Clin. Neurophysiol.* **94**, 183–190.
- Vieth, J., Kober, H., Grummich, P., Pongratz, H., Ulbricht, D., Brigel, C., and Daun, A. (1995) in *Biomagnetism: Fundamental Research and Clinical Applications* (Baumgartner, C., et al., Eds.), pp. 50–54, Elsevier Science, IOS Press, Amsterdam/New York.
- Polhemus Inc., 1 Hercules drive, PO Box 560, Colchester, VT 05446.
- Clarke, J. (1993) in *The New Superconducting Electronics* (Weinstock, H., and Ralston, R. W., Eds.), pp. 123–180, Kluwer Academic, Dordrecht.
- Jaycox, J. M., and Ketchen, M. B. (1981) *IEEE Trans. Magn.* **MAG-17**, 400–403.
- Ketchen, M. B., and Jaycox, J. M. (1982) *Appl. Phys. Lett.* **40**, 736–738.
- Ketchen, M. B., Goubau, W. M., Clarke, J., and Donaldson, G. B. (1978) *J. Appl. Phys.* **44**, 4111–4116.
- Clarke, J., Goubau, W. M., and Ketchen, M. B. (1976) *J. Low Temp. Phys.* **25**, 99–144.
- Zimmerman, J. E., Thiene, P., and Harding, J. T. (1970) *J. Appl. Phys.* **41**, 1572–1580.
- Giffard, R. P., Web, R. A., and Wheatley, J. C. (1972) *J. Low Temp. Phys.* **6**, 533–610.
- Tesche, C. D., and Clarke, J. (1977) *J. Low Temp. Phys.* **27**, 301–331.
- Vrba, J., Betts, K., Burbank, M. B., Cheung, T., Fife, A. A., Haid, G., Kubik, P. R., Lee, S., McCubbin, J., McKay, J., McKenzie, D.,

- Spear, P., Taylor, B., Tillotson, M., Cheyne, D., and Weinberg, H. (1993) *IEEE Trans. Appl. Supercond.* **3**, 1878–1882.
30. Ketchen, M. B., Stawiasz, K. G., Pearson, D. J., Brunner, T. A., Hu, C.-K., Jaso, M. A., Manny, M. P., Parsons, A. A., and Stein, K. J. (1992) *Appl. Phys. Lett.* **61**, 336–338.
  31. Clarke, J. (1996) in H. Weinstock (ed.), *SQUID Sensors: Fundamentals, Fabrication and Applications* (Weinstock, H., Ed.), pp. 1–62, Kluwer Academic, Dordrecht.
  32. Muck, M. (1993) *IEEE Trans. Appl. Supercond.* **3**, 2003–2010.
  33. Braginski, A. I., Krause, H.-J., and Vrba, J. (2000) in *Superconducting Devices, A Volume of Handbook of Thin Film Devices: Frontiers of Research, Technology and Applications* (Francombe, M., and Broussard, P. Eds.), Academic Press, San Diego, in press.
  34. Vrba, J., Fife, A. A., Burbank, M. B., Weinberg, H., and Brickett, P. A. (1982) *Can. J. Phys.* **60**, 1060–1073.
  35. Vrba, J., Betts, K., Burbank, M., Cheung, T., Cheyne, D., Fife, A. A., Haid, G., Kubik, P. R., Lee, S., McCubbin, J., McKay, J., McKenzie, D., Mori, K., Spear, P., Taylor, B., Tillotson, M., and Xu, G. (1995) in *Biomagnetism: Fundamental Research and Clinical Applications* (Baumgartner C. *et al.* Eds.), pp. 521–525, Elsevier Science, IOS Press, Amsterdam.
  36. Williamson, S. J., and Kaufman, L. (1981) *J. Magn. Magn. Mater.* **22**, 129–201.
  37. Knuutila, J. E. T., Ahonen, A. I., Hamalainen, M. S., Kajola, M. J., Petteri Laine, P., Lounasmaa, O. V., Parkkonen, L. T., Simola, J. T. A., and Tesche, C. D. (1993) *IEEE Trans. Mag.* **29**, 3315–3321.
  38. Vrba, J. (1997) Baseline optimization for noise cancellation systems, in *Proceedings of the 19th International Conference IEEE-EMBS, Chicago, IL, Oct. 30 to Nov. 2*, pp. 1240–1243.
  39. Vrba, J., and McKay, J. (1998) *Appl. Supercond.* **5**, 431–439.
  40. Vrba, J., Fife, A. A., and Burbank, M. B. (1981) in *SQUID Applications to Geophysics* (Weinstock, H., and Overton, W. C. Eds.), pp. 31–34, Soc. of Exploration Geophysicists, Tulsa, OK.
  41. McKay, J., Vrba, J., Betts, K., Burbank, M. B., Lee, S., Mori, K., Nonis, D., Spear, P., and Uriel, Y. (1993) Implementation of multichannel biomagnetic measurement system using DSP technology, in *Proceedings of 1993 Canadian Conference on Electrical and Computer Engineering*, Vol. **2**, pp. 1090–1093.
  42. Vrba, J. (1996) in H. Weinstock (ed.), *SQUID Sensors: Fundamentals, Fabrication and Applications* (Weinstock, H., Ed.), pp. 117–178, Kluwer Academic, Dordrecht.
  43. Vrba, J., Anderson, G., Betts, K., Burbank, M. B., Cheung, T., Cheyne, D., Fife, A. A., Govorkov, S., Habib, F., Haid, G., Haid, V., Hoang, T., Hunter, C., Kubik, P. R., Lee, S., McCubbin, J., McKay, J., McKenzie, D., Nonis, D., Paz, J., Reichl, E., Ressler, D., Robinson, S. E., Schroyen, C., Sekachev, I., Spear, P., Taylor, B., Tillotson, M., and Sutherling, W. (1999) in *Recent Advances in Biomagnetism* (Yoshimoto, T., *et al.* Eds.), pp. 93–96, Tohoku Univ. Press.
  44. ter Brake, H. J. M. (2000) in *Applications of Superconductivity* (Weinstock, H., Ed.), pp. 561–639, Kluwer Academic, Dordrecht.
  45. Vacuumschmelze GmbH, Hanau, Germany, shielded room Model AK-3.
  46. Koch, H., PTB, Berlin, Germany, private communication.
  47. Robinson, S. E. (2000) in *Biomag96: Advances in Biomagnetism Research* (Aine, C., *et al.* Eds.), pp. 103–106, Springer-Verlag, Berlin/New York.
  48. Vrba, J. (2000) in *Applications of Superconductivity* (Weinstock, H., Ed.), pp. 61–138, Kluwer Academic, Dordrecht.
  49. Matsuba, H., Shintomi, K., Yahara, A., Irisawa, D., Imai, K., Yoshida, H., and Seike, S. (1995) in *Biomagnetism: Fundamental Research and Clinical Applications* (Baumgartner, C., *et al.* Eds.), pp. 483–489, Elsevier Science, IOS Press, Amsterdam.
  50. Kelha, V. O., Pukki, J. M., Peltonen, R. S., Penttinen, V. J., Ilmoniemi, R. J., and Heino, J. J. (1982) *IEEE Trans. Mag.* **18**, 260–270.
  51. ter Brake, H. J. M., Huonker, R., and Rogalla, H. (1993) *Meas. Sci. Technol.* **4**, 1370–1375.
  52. Vrba, J., Cheung, T., Taylor, B., and Robinson, S. E. (1999) in *Recent Advances in Biomagnetism* (Yoshimoto, T. *et al.*, Eds.), pp. 105–108, Tohoku Univ. Press.
  53. Cheyne, D., Roberts, L. E., Gaetz, W., Bosnyak, D., Weinberg, H., Johnson, B., Nahmias, C., and Deecke, L. (2000) *Biomag96: Advances in Biomagnetism Research* (Aine, C., *et al.*, Eds.), pp. 1130–1133, Springer-Verlag, Berlin/New York.
  54. Zimmerman, J. E. (1977) *J. Appl. Phys.* **48**, 702–710.
  55. Scherg, M., and von Cramon, D. (1985) *Electroencephalogr. Clin. Neurophys.* **62**, 290–299.
  56. Hamalainen, M. S., and Ilmoniemi, R. J. (1984) Interpreting measured magnetic fields of the brain: Estimates of current distributions, Report TKK-F-A559, Low Temperature Laboratory, Helsinki University of Technology, SF-02150 Espoo 15, Finland.
  57. Robinson, S. E., and Vrba, J. (1999) *Recent Advances in Biomagnetism* (Yoshimoto, T., *et al.*, Eds.), pp. 302–305, Tohoku Univ. Press.
  58. Van Veen, B. D., Van Drongelen, W., Yuchtman, M., and Suzuki, A. (1997) *IEEE Trans. Biomed. Eng.* **44**, 867–880.
  59. Mosher, J. C., Lewis, P. S., and Leahy, R. M. (1992) *IEEE Trans. Biomed. Eng.* **39**, 541–557.